Key Points:
- Large fCO_2 undersaturation relative to atmospheric level throughout winter and spring
- Calcium carbonate dissolution acts as a major surface-water fCO_2 loss and sustains undersaturation in Arctic Ocean surface water
- Winter CO_2 sink in leads at high winds exceeds the sink in spring despite larger fCO_2 undersaturation due to phytoplankton bloom

Correspondence to:
A. Fransson,
agneta.fransson@npolar.no

Effects of sea-ice and biogeochemical processes and storms on under-ice water fCO_2 during the winter-spring transition in the high Arctic Ocean: Implications for sea-air CO_2 fluxes

Agneta Fransson[1], Melissa Chierici[2], Ingunn Skjelvan[3], Are Olsen[4], Philipp Assmy[1], Algot K. Peterson[4], Gunnar Spreen[5], and Brian Ward[6]

[1]Norwegian Polar Institute, Fram Centre, Tromsø, Norway, [2]Institute of Marine Research, Tromsø, Norway, [3]Bjerknes Centre for Climate Research, Uni Research Climate, Bergen, Norway, [4]Bjerknes Centre for Climate Research, Geophysical Institute, University of Bergen, Bergen, Norway, [5]Institute of Environmental Physics, University of Bremen, Bremen, Germany, [6]AirSea Laboratory, School of Physics and Ryan Institute, National University of Ireland, Galway, Ireland

Abstract We performed measurements of carbon dioxide fugacity (fCO_2) in the surface water under Arctic sea ice from January to June 2015 during the Norwegian young sea ICE (N-ICE2015) expedition. Over this period, the ship drifted with four different ice floes and covered the deep Nansen Basin, the slopes north of Svalbard, and the Yermak Plateau. This unique winter-to-spring data set includes the first winter-time under-ice water fCO_2 observations in this region. The observed under-ice fCO_2 ranged between 315 μatm in winter and 153 μatm in spring, hence was undersaturated relative to the atmospheric fCO_2. Although the sea ice partly prevented direct CO_2 exchange between ocean and atmosphere, frequently occurring leads and breakup of the ice sheet promoted sea-air CO_2 fluxes. The CO_2 sink varied between 0.3 and 86 mmol C m^{-2} d^{-1}, depending strongly on the open-water fractions (OW) and storm events. The maximum sea-air CO_2 fluxes occurred during storm events in February and June. In winter, the main drivers of the change in under-ice water fCO_2 were dissolution of $CaCO_3$ (ikaite) and vertical mixing. In June, in addition to these processes, primary production and sea-air CO_2 fluxes were important. The cumulative loss due to $CaCO_3$ dissolution of 0.7 mol C m^{-2} in the upper 10 m played a major role in sustaining the undersaturation of fCO_2 during the entire study. The relative effects of the total fCO_2 change due to $CaCO_3$ dissolution was 38%, primary production 26%, vertical mixing 16%, sea-air CO_2 fluxes 16%, and temperature and salinity insignificant.

1. Introduction

The ice cover in the Arctic Ocean has decreased during the last decades, manifested in particular as an extensive transition from multiyear ice (MYI) to first-year ice (FYI) [e.g., *Serreze and Stroeve*, 2015; *Meier et al.*, 2014; *Lindsay and Schweiger*, 2015]. As the summer sea-ice cover is decreasing, larger areas have only seasonal sea-ice cover and waters that are exposed to the atmosphere during the Arctic summer, as in the Antarctic Ocean. This open water is favorable for sea-air carbon dioxide (CO_2) exchange. The direction and magnitude of the net sea-air CO_2 exchange depend on salinity, temperature, wind speed, and the difference in CO_2 partial pressure between water and atmosphere. So far, estimates of sea-air CO_2 fluxes during the Arctic summer have shown that the Arctic Ocean acts as an atmospheric CO_2 sink [e.g., *Fransson et al.*, 2009; *Bates and Mathis*, 2009; *Schuster et al.*, 2013; *Yasunaka et al.*, 2016].

The surface-water fugacity of CO_2 (fCO_2) in the Arctic Ocean varies due to physical processes (e.g., temperature, mixing of waters, sea-ice processes, and freshwater addition) and biological processes (e.g., primary production and remineralization of organic carbon) [e.g., *Fransson et al.*, 2009]. In upwelling areas such as the Bering Sea and Arctic polynyas, high CO_2 in the surface promotes CO_2 release from the ocean to the atmosphere [e.g., *Yager et al.*, 1995; *Fransson et al.*, 2006, 2009; *Else et al.*, 2012]. In parts of the Arctic Ocean, such as the Canadian Arctic Archipelago, the major driver for the surface-water fCO_2 change is biological [e.g., *Chierici et al.*, 2011; *Fransson et al.*, 2013]. In addition, several studies have shown the importance of CO_2-rich sea-ice brine for mediating vertical transport of CO_2 in the water column, often referred as the sea-ice brine CO_2 pump [e.g., *Omar et al.*, 2005; *Rysgaard et al.*, 2007, 2009; *Miller et al.*, 2011; *Fransson et al.*,

2013]. Although the sea-ice cover hampers direct CO_2 flux between air-water interfaces, recent studies have shown that processes within the sea ice indirectly promote sea-air CO_2 [e.g., *Rysgaard et al.*, 2007, 2013; *Nomura et al.*, 2010; *Fransson et al.*, 2013; *Delille et al.*, 2014]. While sea ice and brine are forming, salinity and chemical substances such as CO_2 become concentrated. These concentrated components can cause supersaturation in the ice with respect to CO_2 and minerals, such as calcium carbonate ($CaCO_3$) [*Assur*, 1960]. Precipitation of $CaCO_3$ from the brine produces $CO_2(aq)$ and reduces total alkalinity (AT) in the brine (equation (1)).

$$[Ca^{2+} + 2HCO_3^- \rightarrow CaCO_3(s) + H_2O + CO_2(aq)]. \tag{1}$$

Ikaite is a form of $CaCO_3$, which precipitates in both Arctic and Antarctic sea ice [e.g., *Dieckmann et al.*, 2008, 2010; *Rysgaard et al.*, 2011]. When solid ikaite dissolves in the surface water, CO_2 is consumed and alkalinity increases (equation (1)). Brine volume depends on ice temperature and salinity, and when brine volume is larger than 5%, the sea-ice layer becomes permeable [*Weeks and Ackley*, 1986; *Golden et al.*, 1998, 2007] so that brine as well as ikaite can exchange with underlying seawater through gravity drainage [*Notz and Worster*, 2009]. Consequently, the sea ice can become a source of either CO_2 or alkalinity to the underlying water [*Rysgaard et al.*, 2007, 2009, 2012; *Nedashkovsky et al.*, 2009; *Geilfus et al.*, 2012, 2016; *Fransson et al.*, 2013]. Due to the rejection of brine, fCO_2 can become higher than the atmospheric and/or underlying water fCO_2, which can result in CO_2 outgassing from the ice to the atmosphere and/or to the underlying water [e.g., *Papadimitriou et al.*, 2004; *Rysgaard et al.*, 2007, 2013; *Miller et al.*, 2011; *Geilfus et al.*, 2012; *Fransson et al.*, 2009, 2013]. On the other hand, brine that contains ikaite can escape from the sea ice to underlying water through brine channels, where ikaite dissolves, consuming CO_2 [e.g., *Fransson et al.*, 2013; *Geilfus et al.*, 2016]. In addition, in spring, primary production decreases fCO_2, and the ice and its meltwater act as a sink of atmospheric CO_2 [e.g., *Rysgaard et al.*, 2007, 2013; *Fransson et al.*, 2001, 2013; *Nomura et al.*, 2013]. Moreover, studies in the Canadian Arctic Archipelago showed exchange of CO_2 at openings in the ice cover through leads and cracks in the ice in winter [*Else et al.*, 2013].

Ship-based high-frequency sea-surface fCO_2 measurements, typically based on infrared determination of the CO_2 concentration in an equilibrator headspace, are frequently used to estimate air-sea CO_2 fluxes at regional and global scales [e.g., *Takahashi et al.*, 2009; *Le Quéré et al.*, 2015]. However, such data are scarce in the Arctic Ocean and particularly in ice-covered waters. *Fransson et al.* [2009] carried out some of the first high-frequency sea-surface fCO_2 measurements in the Arctic Ocean, in the ice-covered Northwest Passage from the Labrador Sea to the Chukchi Sea. They found large variability in surface fCO_2 and sea-air CO_2 fluxes where most of the variability could be explained in terms of freshwater addition (sea-ice melt and river run-off), primary production, and upwelling. *Else et al.* [2012, 2013] measured fCO_2 continuously under the ice using a ship as a platform during a full sea-ice cycle in a flaw lead in the Canadian Arctic Archipelago, and that is one of few winter-time fCO_2 measurements in the ice-covered part of the Arctic Ocean.

In general, fCO_2 data in the Arctic Ocean are scarce. In this study, we present unique measurements of fCO_2 under sea ice obtained during a 5 month drift over the deep Arctic basin (Nansen Basin) and the Yermak Plateau north of Svalbard from January (winter) to end of June (spring) [*Granskog et al.*, 2016]. As evaluated from version 4 of the Surface Ocean CO_2 Atlas [*Bakker et al.*, 2016, www.socat.info], no fCO_2 data have previously been obtained in this area. Our data are also unique for the Arctic Ocean since it was collected in the period with the least data, from January to June. R/V *Polarstern* passed the area and performed underway fCO_2 measurements toward the end of the period covered by the current study, and there may be a few coinciding data points (expocode: 06AQ20150519, 15 May to 27 June 2015). We quantify the major monthly biogeochemical drivers of the observed fCO_2 variability during a 5 month period using ancillary surface-water data. The sea-air CO_2 flux is estimated and related to sea-ice concentration and open-water fraction, and we discuss the effects of storm events on the fCO_2 and the sea-air CO_2 flux.

2. Study Area

The study took place during the Norwegian young sea ICE (N-ICE2015) expedition with R/V *Lance*, covering the area from the deep Nansen Basin to the slopes north of Svalbard and the Yermak Plateau (80°N–83°N, 8°E–28°E; Figures 1a and 1b) from 15 January 2015 to 22 June 2015 [*Granskog et al.*, 2016]. We drifted with four different ice floes from January (winter) to June (spring) 2015, and fCO_2 was continuously
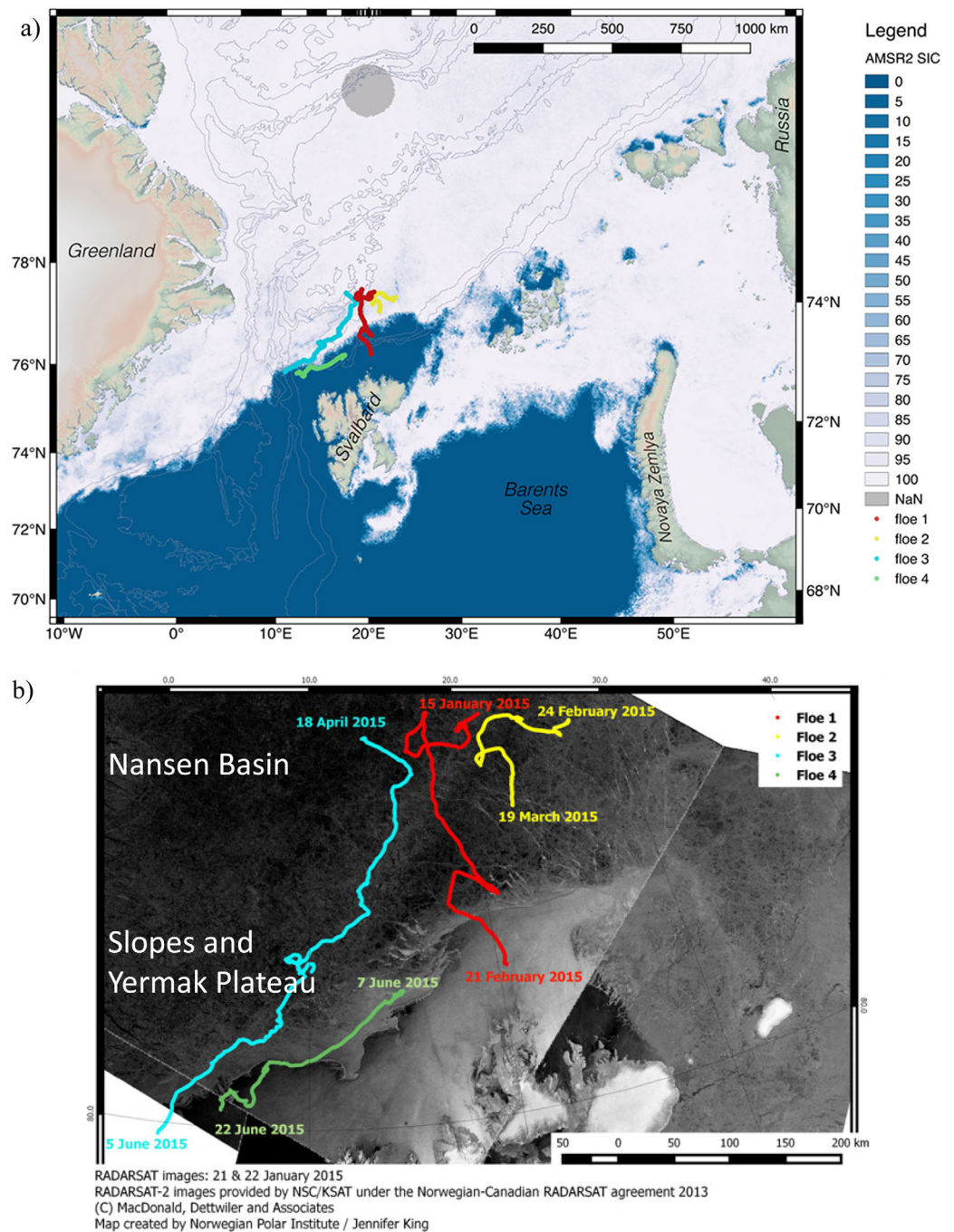
Figure 1. (a) Location of the N-ICE2015 expedition (colored trajectories) in the Arctic Ocean and adjacent seas, including floes and ice drift; Floe 1 (red), Floe 2 (yellow), Floe 3 (blue), and Floe 4 (green). The background shows sea-ice concentrations on 6 February 2015 (the day of a major storm event) obtained from the AMSR2 satellite radiometer [Spreen et al., 2008]. The grey lines are 1000 m contours of the bathymetry. (b) Study area with floes and ice drift through the deep Nansen Basin, the slopes north of Svalbard, and the Yermak Plateau.

Table 1. Start and End Dates for Each Floe, Season, and the Type of Study Area Based on Bathymetry

Date (Start, End)	Floe#	Season	Area
15 Jan–21 Feb	1	Winter	Nansen Basin (>3000 m) and slope (1500–3000 m)
24 Feb–19 Mar	2	Winter	Nansen Basin (>3000 m) and slope (1500–3000 m)
18 Apr–5 Jun	3	Spring	Yermak Plateau (<1500 m) and slope (1500–3000 m)
7 Jun–22 Jun	4	Spring	Yermak Plateau (<1500 m) and slope (1500–3000 m)

measured. In winter, we drifted over the deep Nansen Basin (depth > 3000 m) and over the shallow slope areas toward Svalbard. In spring, the drift was mostly over the slope (Table 1). Table 2 provides an

Table 2. The Meteorological Properties at 10 m Above Sea-Ice Are Shown for Each Floe[a]

Floe#		T air (°C)	P air (hPa)	RH (%)	u (m s^{-1})
1	**Mean**	**−27**	**995**	**75**	**7.3**
1	(min, max)	(−40, 0)	(969, 1024)	(65, 99)	(0.2, 23)
2	**Mean**	**−20**	**997**	**87**	**5.7**
2	(min, max)	(−35, −1.9)	(966, 1024)	(74, 98)	(0,1, 19)
3	**Mean**	**−18**	**1014**	**87**	**6.2**
3	(min, max)	(−26, −0.2)	(997, 1032)	(56, 99)	(0.0, 15)
4	**Mean**	**−0.64**	**1011**	**94**	**6.7**
4	(min, max)	(−1.6, 0.4)	(999, 1022)	(79, 99)	(0.7, 17)

[a]The mean, minimum, and maximum (min, max) air temperature (T air, °C), air pressure (P air, hPa), relative humidity (RH, %), and wind speed (u, m s^{-1}) are shown [*Hudson et al.*, 2015]. P air is from 22 m height at the same location as the fCO$_2$ air intake.

overview of average meteorological conditions during the four drifts [*Hudson et al.*, 2015].

Frequent storms occurred during the study and are described in more detail by *Cohen et al.* [2017] in Table 3 and Figures 2a and 2b). During Floe 1, there were synoptic storms in February (e.g., M2 and M3), when air temperatures increased by more than 30°C in 1 day (Tables 2 and 3) [*Hudson et al.*, 2015; *Cohen et al.*, 2017]. Generally, th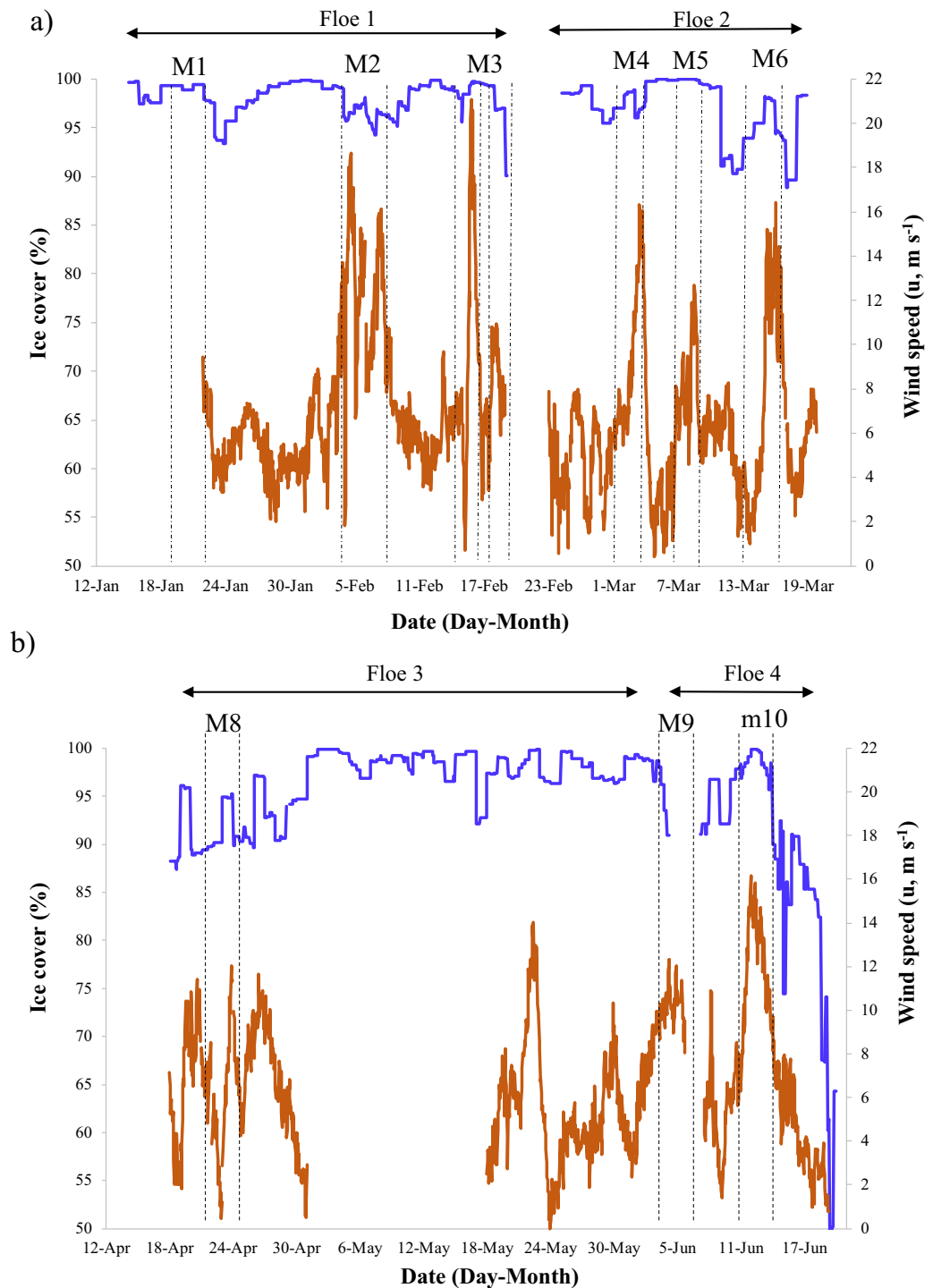e air temperatures in winter were low with a mean of −27°C and a minimum of below −40°C (Floe 1). In spring, the air temperature increased to a mean of −18°C (Floe 3) and a minimum of −0.64°C (Floe 4).

In winter, surface waters were dominated by cold and fresh Polar Surface Water (PSW, $\Theta < 0$°C and $\sigma_0 < 27.70$) in the upper 100 m (Figures 3a and 3b), described in detail by *Meyer et al.* [2017a, 2017b]. In late spring, the upper 100 m were dominated by a mix of Polar Surface Water and warm Polar Surface Water (PSWw, $\sigma_0 < 27:70$ and $\Theta > 0$°C), with occasional intrusions of Atlantic Water (AW, $\Theta > 2$°C and $27.70 < \sigma_0 < 27.97$) close to the surface [*Meyer et al.*, 2017a, 2017b, Figure 7]. The observed sea-surface temperature (SST) corresponded to the freezing point of seawater, approximately −1.8°C, between January and May, and increased to above 0.7°C in June (Table 4 and Figure 4a). In January to mid-May, surface-water salinity was above 34 and in June, vertical mixing of warm Atlantic water caused bottom ice melt, and consequently a decrease of sea-surface salinity of 32.7 [*Meyer et al.*, 2017a, 2017b, Figures 3b and 4b].

The fraction of open water (OW) around R/V *Lance* varied throughout the study, with a winter maximum of 7% and a spring maximum of 53% in June (Figures 2a and 2b). Increased open-water fractions mostly coincided with storm events defined by *Cohen et al.* [2017] (Figures 2a and 2b and Table 3).

Table 3. Storm Events Summary for All Floes[a]

Season/Floe#	Date Start Time (UTC)	Date End Time (UTC)	Storm Name	Wind Speed Peak (m^{-1})	Pressure Min (hPa)	Temperature (°C) Min	Temperature (°C) Max
Winter/Floe1	21 Jan, 21:00	22 Jan, 07:00	M1	10.8	990	−27	−3.1
Winter/Floe1	3 Feb, 11:00	8 Feb, 21:00	M2	22	967	−35.5	−1.4
Winter/Floe1	13 Feb, 04:00	13 Feb, 09:00	m1	10	989	−36.4	−26
Winter/Floe1	15 Feb, 12:00	16 Feb, 17:00	M3[c]	23	976	−34.1	−0.2
Winter/Floe1	17 Feb, 16:00	21 Feb, 04:00[b]	M3[c]	11.9	976	−34.1	−0.2
Winter/Floe1	22 Feb, 08:00[b]	23 Feb, 01:00[b]	m2[b]	10.3[b]	980[b]	−32.3[b]	−20.9[b]
Winter/Floe2	25 Feb, 06:00[b]	25 Feb, 20:00[b]	m3[b]	8.7[b]	1001[b]	−29.1[b]	−15.5[b]
Winter/Floe2	2 Mar, 10:00	4 Mar, 01:00	M4	16.8	998	−25.6	−3.1
Winter/Floe2	7 Mar, 08:00	8 Mar, 18:00	M5	14.2	966	−19.5	−1.9
Winter/Floe2	14 Mar, 21:00	16 Mar, 23:00	M6	19.2	966	−31.3	−2.2
Spring/Floe3	23 Apr, 10:00[b]	24 Apr, 12:00[b]	m4[b]	14.3[b]	1009[b]	−22.9[b]	−14.3[b]
Spring/Floe3	25 Apr, 04:00	27 Apr, 23:00	M7	12.6	1021	−20.3	−9.7
Spring/Floe3	6 May, 23:00[b]	8 May, 02:00[b]	m5[b]	10	1012	−17.3	−13.3
Spring/Floe3	9 May, 16:00[b]	10 May, 19:00[b]	m5[b]	10.4	1012	−17.3	−13.3
Spring/Floe3	16 May, 12:00	16 May, 23:00	m6	12.3	1003	−15	0.3
Spring/Floe3	21 May, 10:00	23 May, 01:00	m7	15.4	1004	−13.5	−9
Spring/Floe4	29 May, 17:00	30 May, 05:00	m8	10.6	1012	−4.9	−2.2
Spring/Floe4	2 Jun, 15:00	6 Jun, 13:00[b]	M8	13.7	1003	−3	0.5
Spring/Floe4	8 Jun, 1:00	8 Jun, 6:00	m9	12	1000	0.2	1.5
Spring/Floe4	11 Jun, 2:00	14 Jun, 5:00	m10	17.3	1002	−2.9	0.7

[a]"M" means major storm and "m" minor storm. "Min" means minimum and "Max" means maximum (adopted after *Cohen et al.*, [2017]).
[b]Values are from shipboard instruments (meteorological tower data not available).
[c]The storm had two separate periods of high wind.

Figure 2. The ice concentration estimated over a 44 × 44 km^2 box (%; blue line, left y axis) and wind speed (u, m s^{-1}; orange line, right y axis) along drift of (a) Floe 1 and Floe 2 and (b) Floe 3 and Floe 4. The double arrows indicate the start and end of the study on each floe. The period between Floe 1 and Floe 2 has data gaps caused by the time used to relocate R/V Lance. The areas within the dotted lines and M1–M9 and m10 are storm events (Table 3) defined by *Cohen et al.*, [2017].

However, occasionally in February–March, there was a time lag of 1–3 days between the maximum wind speed and the maximum OW. In April and May, the response time was within 12–24 h. Occasionally, OW decreased due to closing of leads during short pulses of high winds and changes in wind direction, particularly in March.
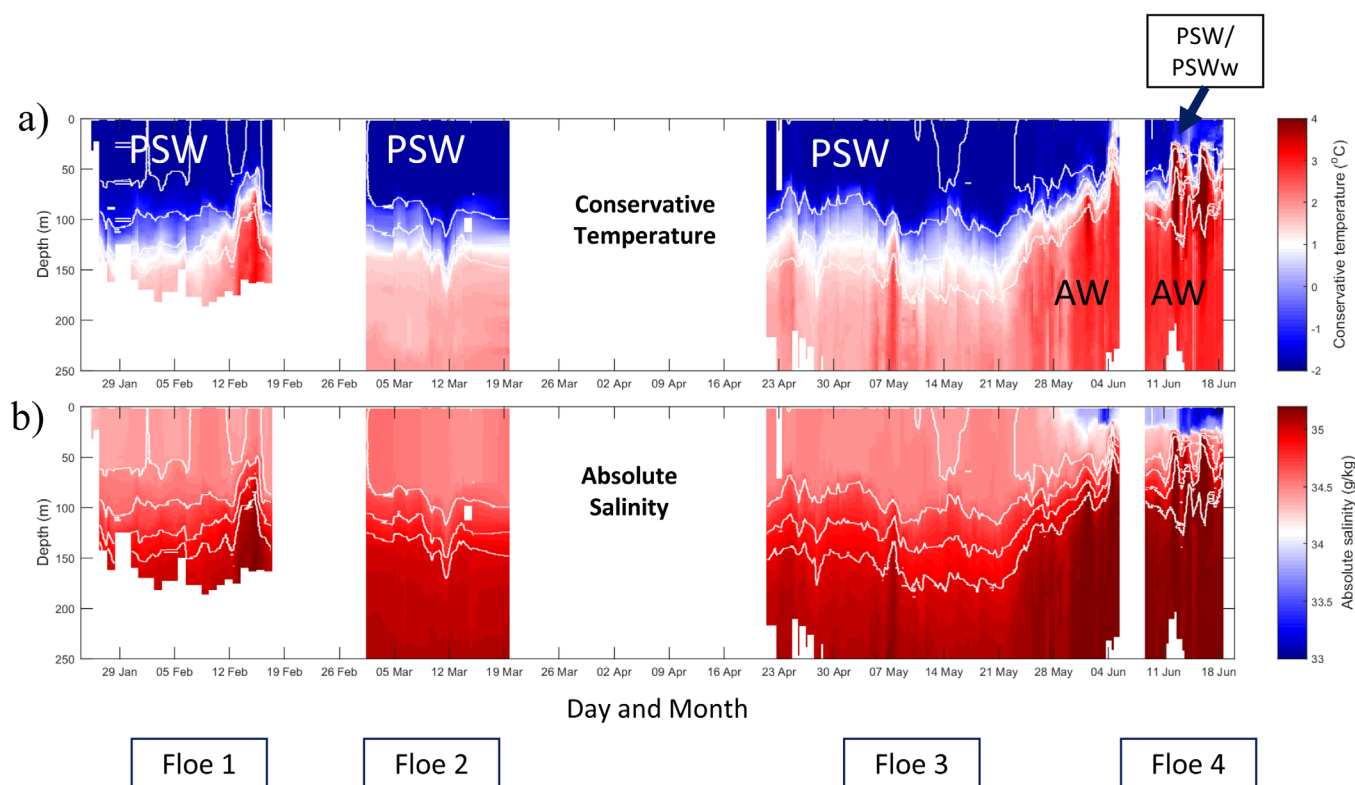
Figure 3. Hydrography and water masses in the upper 250 m during the N-ICE2015 from January to June, showing seawater (a) conservative temperature (°C) and (b) absolute salinity (g kg^{-1}) [*McDougall et al.*, 2012] obtained by microstructure profilers [*Meyer et al.*, 2016, 2017a, 2017b]. Key water masses are indicated; Polar Surface Water (PSW), warm Polar Surface Water (PSWw), and Atlantic Water (AW) (details of water masses in *Meyer et al.* [2017a, 2017b, Figure 7]). White isolines correspond to selected potential density contours: 27.6, 27.7, 27.8, and 27.85 kg m^{-3}. Figures are adopted from *Meyer et al.* [2017a, 2017b].

The ice pack was composed primarily of young ice (YI) with little snow, first-year ice (FYI) and second-year ice (SYI) [*Granskog et al.*, 2017], with thick snow (0.3–0.5 m) [*Rösel et al.*, 2016a]. In the region, modal ice thickness was about 1.3–1.5 m [*Rösel et al.*, 2016b].

3. Data and Methods

The fCO$_2$ data were obtained by infrared analysis of equilibrator headspace samples. The specific instrument was supplied by General Oceanics® and designed following the principles presented by *Pierrot et al.* [2009] using two-stage showerhead equilibration and a LICOR® 7000 nondispersive infrared detector. The system was calibrated using three reference gases with approximate values of 250, 350, and 450 ppm, traceable to reference standards provided by NOAA/ESRL (National Oceanic and Atmospheric Administration-Earth System Research and Laboratory; see *Pierrot et al.* [2009] for a more thorough description of the system). Standards were run every third hour. The zero and span of the LICOR were set approximately once a day. The seawater was supplied from an intake located midships, at approximately 5 m water depth. Temperature was recorded in the equilibrator and the surface-water intake using 1521 temperature probes from Hart Scientific, with an accuracy of 0.01°C. Atmospheric xCO$_2$ was measured in air samples, pumped from an air intake located in the crow's nest, approximately 30 m above sea level. Wind speed, air temperature, and air humidity (Tables 2 and 3) were obtained from the ship's met-station and a weather mast located at the ice camp 300–400 m away from the ship [*Hudson et al.*, 2015]. Air pressure was recorded by a high-precision Druck barometer mounted at the air intake in the crow's nest.

Sea-ice concentration and open-water fraction were obtained from the AMSR2 microwave radiometer on the JAXA GCOM-W satellite. Sea-ice concentrations were derived from the 89 GHz channels, which allow a daily full global coverage of all sea-ice areas on a 6.25 × 6.25 km^2 grid [*Spreen et al.*, 2008, www.seaice.uni-

bremen.de/amsr2]. The mean sea-ice concentration for a square of 43.75×43.75 km^2 (7×7 grid cells) with R/V *Lance* in the center pixel was calculated on an hourly basis. The GPS position of R/V *Lance* was used to identify the center grid cell in the ice concentration data set. The resulting time series is the sea-ice area fraction of a square of approximately 44×44 km^2 along the drift paths of the four N-ICE2015 floes. The open-water fraction is one minus the sea-ice area fraction.

3.1. Calculation of Surface-Water fCO$_2$

The fugacity of CO$_2$ (fCO$_2$) is similar to the partial pressure, but takes into account the nonideal nature of the CO$_2$ gas. The General Oceanics® system measures the mole fraction of CO$_2$ (xCO$_2$) in the equilibrator headspace sample, and this is converted to fCO$_2$. This conversion is well described by *Wanninkhof and Thoning* [1993] and summarized here

$$fCO_2 = xCO_2^{eq}(P_T - p_{H2O})\exp\left(p^{eq}\frac{B_{12} + 2\delta_{12}}{RT^{eq}}\right)\exp[0.0423(SST - T^{eq})], \qquad (2)$$

where fCO$_2$ refers to the value in seawater, xCO$_2^{eq}$ refers to the equilibrator, P$_T$ is the total pressure, p$_{H2O}$ is the vapor pressure at the equilibrator temperature T^{eq}, SST is the sea-surface temperature from the seawater intake, and R is the gas constant. The increase in fCO$_2$ from heating over the tubing path length between the water intake and the equilibrator is $(\delta \ln fCO_2/\delta T) = (0.0423 \pm 0.0002)°C^{-1}$, as determined by *Takahashi et al.* [1993]. The terms B$_{11}$ and δ_{12} describe the second virial coefficient of pure CO$_2$ and a correction for air-CO$_2$ mixture [*Weiss*, 1974], respectively.

Occasionally, and particularly in January and February, the room housing the seawater inlet was temperature-controlled to prevent freezing and clogging of the intake. Since this affected the temperature of the incoming water, it was decided not to use any of the surface-water intake temperatures as SST. Rather, a combination of ship-CTD (conductivity-temperature-depth) temperature data from 5 m depth [*Dodd et al.*, 2016; *Meyer et al.*, 2017a, 2017b] and measurements of in situ temperature from 1–2 m depth from an on-ice turbulence mast was used in equation (2). The mast was deployed through a hole in the ice, approximately 300–400 m away from the ship. Sensors included high-precision SeaBird temperature and salinity sensors for sampling at 5 m below the ice surface. Data were sampled at 3 Hz, and averaged to 5 min for this study (see *Peterson et al.* [2017] for a detailed description). The CTD temperatures were point observations and were used to adjust the temperatures from the on-ice turbulent mast. Adjustments were in the range of 0.001–0.015°C. When temperatures from the on-ice turbulent mast were not available (e.g., from January to the first week of March) CTD temperatures from 5 m depth [*Dodd et al.*, 2016] were used, linearly extrapolated between the points, since the seawater temperature was approximately constant at freezing temperatures. Further, due to the heating of the water inlet room, the equilibrator temperature was occasionally substantially larger than the true SST. To limit errors in fCO$_2$ caused by excessive temperature corrections, only fCO$_2$ data with temperature differences (between SST and equilibrator) of less than 3°C are presented here (Integrated Carbon Observing System (ICOS) recommendation for fCO$_2$ measurements class 1 in areas close to the ice edge). The uncertainty due to temperature correction in fCO$_2$ caused by a warming of 3°C was maximum 3.5 µatm, using *Takahashi et al.* [1993] and estimates by CO2SYS calculations [*Pierrot et al.*, 2006]. Salinity data were obtained from a combination of the under-ice turbulence mast [*Meyer et al.*, 2016; *Peterson et al.*, 2017] and CTD data [*Dodd et al.*, 2016; *Meyer et al.*, 2017a, 2017b].

The dissolved inorganic carbon (DIC) and total alkalinity (A$_T$) samples were analyzed at the Institute of Marine

Table 4. The Mean Values and Standard Deviation (SD) for the Physical (Salinity, S and Temperature, SST) and Chemical Properties (fCO$_2$) in the Upper 5 m for the Different Floes During the N-ICE2015 Expedition[a]

Floe	S (0–5 m) Mean, SD (Min, Max)	SST (0–5 m, °C) Mean, SD (Min, Max)	fCO$_2$ (0–5 m, µatm) Mean, SD (Min, Max)
1	34.30, ±0.05 (34.21, 34.35)	−1.83, ±0.03 (−1.88, −1.79)	283, ±10 (266, 315)
2	34.33, ±0.04 (34.28, 34.41)	−1.86, ±0.01 (−1.88, −1.82)	283, ±4 (274, 294)
3	34.25, ±0.16 (33.60, 34.34)	−1.83, ±0.02 (−1.87, −1.73)	272, ±26 (182, 308)
4	33.29, ±0.39 (32.69, 33.80)	−1.34, ±0.58 (−1.78, 0.76)	189, ±15 (153, 219)

[a]fCO$_2$ refers to the fugacity of carbon dioxide in surface water.
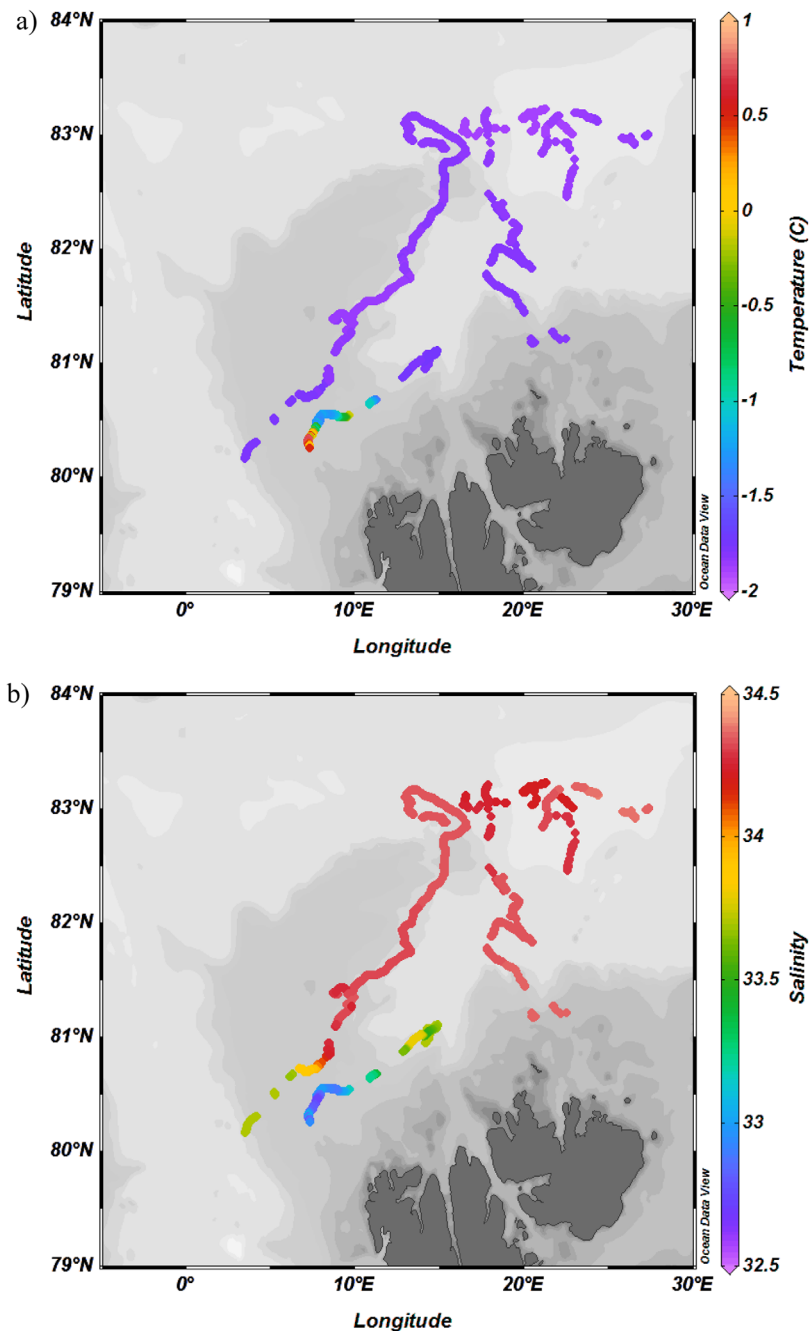
Figure 4. Spatial variability of surface-water (a) temperature (°C), and (b) salinity, in the upper 5 m for the entire study. Gray-shaded gradients denote bathymetry from dark gray (shallow) to light gray (deep).

Research (IMR Tromsø, Norway) following the method described in *Dickson et al.* [2007]. DIC was determined using gas extraction of acidified samples followed by Coulometric titration and photometric detection using a Versatile Instrument for the Determination of Titration Alkalinity (VINDTA 3D, Marianda, Germany). The A_T was determined by potentiometric titration with 0.1 N hydrochloric acid using a Versatile Instrument for the Determination of Titration Alkalinity (VINDTA 3S, Marianda, Germany). Routine analyses of Certified Reference Materials (CRM, provided by A. G. Dickson, Scripps Institution of Oceanography, USA) ensured the accuracy of the measurements, which was better than ± 1 and ± 2 μmol kg^{-1} for DIC and A_T, respectively. We used A_T, DIC, and nutrients as input parameters in a CO_2-chemical speciation model (CO2SYS program) [*Pierrot et al.*, 2006] to calculate fCO$_2$ based on the carbonate system dissociation
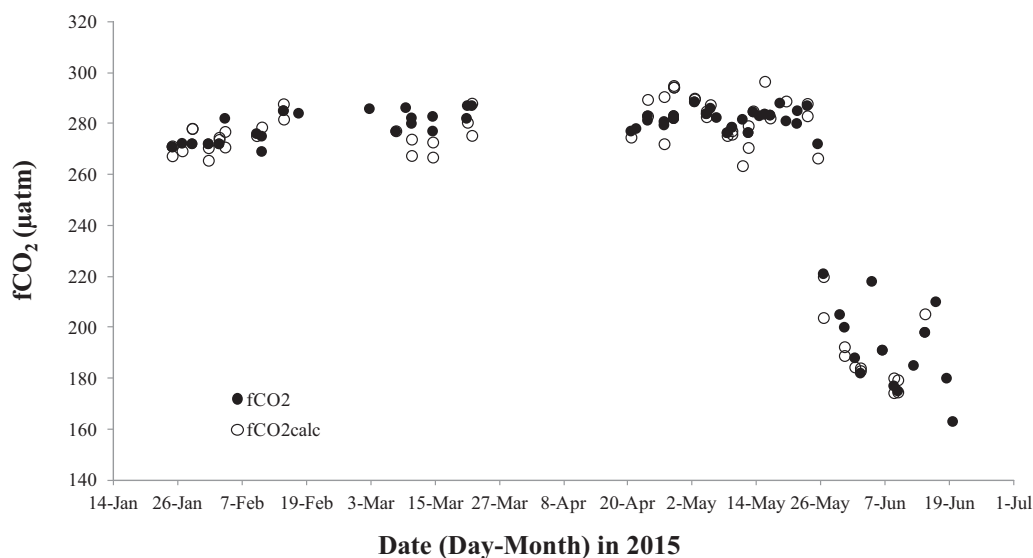
Figure 5. The observed $f\text{CO}_2$ (μatm; black filled circles) and the calculated $f\text{CO}_2$ ($f\text{CO}_2$ calc, μatm; open circles,) from total alkalinity (A_T) and dissolved inorganic carbon (DIC) sampled at 5 m depth using the CO2SYS program [*Pierrot et al.*, 2006] from January to June 2015.

constants (K*1 and K*2) estimated by *Mehrbach et al.* [1973], modified by *Dickson and Millero* [1987] and the HSO_4^- dissociation constant from *Dickson* [1990].

Measurements of A_T and DIC in surface samples (from the seawater intake or CTD casts) were used to calculate $f\text{CO}_2$ to compare with the $f\text{CO}_2$ measurements of the underway system (Figure 5). We performed a regression analysis between measured $f\text{CO}_2$ at SST and calculated $f\text{CO}_{2\text{calc}}$ (from pairs of A_T and DIC). The linear regression resulted in a root mean standard error (rmse) in $f\text{CO}_2$ of ± 7 μatm, a slope of 0.997, and a coefficient of determination (r^2) of 0.999 based on 53 data points. The rmse of ± 7 μatm includes the effect of the location, sampling, warming of the measured $f\text{CO}_2$, analytical uncertainties in the determination of A_T and DIC, equilibrium constants as well as any error associated with carbonate-chemistry calculations (CO2SYS). However, the sum of all uncertainties includes compensatory effects causing a net error of ± 7 μatm, which in fact could be larger than the estimated rmse in this method.

Water samples for nutrients were collected in acid-washed 125 mL bottles (Nalgene®, Rochester, NY, USA), fixed with 0.2 mL chloroform and stored refrigerated until analysis [*Assmy et al.*, 2016]. The nutrient samples were analyzed at IMR, Bergen, and the following nutrients: nitrite ($[NO_2^-]$), nitrate ($[NO_3^-]$), phosphate ($[PO_4^{3-}]$) were measured spectrophotometrically at 540, 540, and 810 nm, respectively, on a modified Scalar autoanalyser [*Bendschneider and Robinson*, 1952] (RFA methodology). The detection limits were 0.06 mmol m^{-3} for $[NO_2^-]$, 0.04 mmol m^{-3} for $[NO_3^-]$, and 0.06 mmol m^{-3} for $[PO_4^{3-}]$.

Chlorophyll-a samples were filtered onto 25 mm GF/F filters (Whatman), extracted on board with 100% methanol for 12 h at 5°C and measured fluorometrically using a Turner Fluorometer 10-AU (Turner Design, Inc.) [*Assmy et al.*, 2016]. Phaeopigments were measured by fluorescence after acidification with 5% HCl [*Holm-Hansen and Riemann*, 1978].

3.2. Calculations of Sea-Air CO$_2$ Flux
Using the measured $f\text{CO}_2$, we calculated the sea-air CO$_2$ flux, F, according to the gas flux formulation (equation (3)),

$$F = K_0 k \left(f\text{CO}_2 - f\text{CO}_2^{air} \right) \ OW, \tag{3}$$

$$k = 0.251 u^2 \sqrt{\frac{660}{Sc}}, \tag{4}$$

where K_0 is the solubility (mol m^{-3} atm^{-1}), k is the transfer velocity (cm h^{-1}) for sea-air CO$_2$ exchange, u is the wind speed (m s^{-2}), OW is the open-water fraction, and $f\text{CO}_2^{air}$ and $f\text{CO}_2$ are the atmospheric and sea

surface $f\mathrm{CO}_2$, respectively. K_0 was calculated according to *Weiss* [1974] using the measured SST and salinity values. The transfer velocities (k) and the Schmidt number (Sc) were calculated according to *Wanninkhof* [2014] for monthly and daily average observed wind speed (equation (4)) and are based on wind speed (u) at 10 m height above sea-ice surface obtained from the weather-mast meteorological data [*Hudson et al.*, 2015]. The transfer velocity can be affected by the sea ice itself, which can generate turbulence, convection, and current shear [*McPhee*, 2005]. Sea ice related to open water (e.g., leads and cracks) may also attenuate wind-driven turbulence by the reflection and scattering of wind waves [*Masson and LeBlond*, 1989]. However, in ice-covered oceans and in winter, these interactions on a spatiotemporal range are limited and not accounted for here. The $f\mathrm{CO}_2^{air}$ was set to its average of 406 μatm, based on all our $x\mathrm{CO}_2^{air}$ measurements in this study. We converted the dry atmospheric mole fractions, $x\mathrm{CO}_2^{air}$ to the atmospheric partial pressure of CO_2 ($p\mathrm{CO}_2^{air}$) in wet air according to equation (5),

$$pCO_2^{air} = xCO_2^{air}(slp - p_{H2O}),\tag{5}$$

where slp is the sea-level pressure and p_{H2O} the vapor pressure at the observed SST and salinity, calculated according to *Weiss and Price* [1980]. Values of $p\mathrm{CO}_2^{air}$ were converted to $f\mathrm{CO}_2^{air}$ according to *Weiss* [1974], following the procedure described in *Dickson et al.* [2007].

3.3. Calculations of Drivers Effecting Under-Ice Water $f\mathrm{CO}_2$

We estimated the effect of different drivers on the monthly change in the observed surface-water $f\mathrm{CO}_2$ ($\frac{df\,CO2obs}{dt}$) and the previous month $f\mathrm{CO}_2$ ($f\mathrm{CO}_{2\,t-1}$) following a similar approach as used elsewhere [e.g., *Chierici et al.*, 2006; *Fransson et al.*, 2006, 2013]. Equations (6–9) below describe the effect of temperature change ($\frac{df\,CO2_T}{dt}$), salinity change ($\frac{df\,CO2S}{dt}$), biological processes ($\frac{df\,CO2\;bio}{dt}$), vertical mixing ($\frac{df\,CO2\;mix}{dt}$), the sea-air CO_2 flux ($\frac{df\,CO2flux}{dt}$), and the effect of CaCO_3 dissolution or precipitation ($\frac{df\,CO2CaCO3}{dt}$) in the upper 10 m (H) between January and April. In May and June, the surface-mixed layer shoaled to 5 m [*Meyer et al.*, 2017a, 2017b] and is used for calculations during this period. The effect of temperature was estimated using the relationship described by *Takahashi et al.* [1993] where a 1°C change results in a 4.23% change in $f\mathrm{CO}_2$. The monthly mean values of DIC and the Revelle factor for each month (R) were used to convert the change in sea-air CO_2 flux to a $f\mathrm{CO}_2$ change, and the stoichiometric ratio between carbon and nitrogen (C/N) was used to convert the monthly nitrate change ($\frac{dNO3}{dt}$) to carbon equivalents, and DIC and R to convert carbon to a $f\mathrm{CO}_2$ change. We used the C/N ratio of 5.7 ± 1.3 estimated by *Assmy et al.* [2017] for our area and time of study. The effect of salinity change was estimated using CO2SYS, where 1 salinity unit change contributed to a change in $df\mathrm{CO}2_S$ of 4 μatm. In our study, salinity was relatively constant throughout the period except for the freshening between May and June.

$$\frac{dfCO2obs}{dt} = \frac{1}{dt}(dfCO2_T + dfCO2_S + dfCO2_{biomix} + dfCO2_{flux} + dfCO2_{CaCO3}),\tag{6}$$

$$\frac{dfCO2_T}{dt} = fCO2_{t-1} \cdot e^{0.0423} \cdot \frac{dT}{dt},\tag{7}$$

$$\frac{dfCO2_{bio}}{dt} = \left(\frac{\partial fCO2}{\partial NO3}\frac{dNO3}{dt}\right)/DIC \cdot {}^{C}/_{N} \cdot R \cdot fCO2_{\;t-1},\tag{8}$$

$$\frac{dfCO2_{flux}}{dt} = \frac{R \cdot fCO2_{t-1} \cdot fCO2_{flux}}{(DIC \cdot H)},\tag{9}$$

$\frac{dfCO2_{CaCO3}}{dt}$ was estimated from the residual between the sum of all other drivers and $\frac{dfCO2obs}{dt}$. The residual is explained by changes in CaCO_3 dissolution/formation (see equation (1)), CO_2 addition from brine rejection, or CO_2 addition from horizontal advection. From this follows an assumption that the contribution of bacterial respiration in the upper 10 m was negligible. A negative change denotes a $f\mathrm{CO}_2$ loss larger than the observed decrease. The function $\frac{dfCO2\;mix}{dt}$ is equal to $\frac{dfCO2\;bio}{dt}$ when $\frac{dfCO2\;bio}{dt} > 0$, and equal to 0 when to $\frac{dfCO2\;bio}{dt} \leq 0$.

The cumulative error of all uncertainties in the effects of drivers was calculated based on the sum of the quadratic function of the analytical precision in surface-water temperature (T), salinity (S), nitrate concentrations (NO_3), and $f\mathrm{CO}_2$ (see section 3), the standard deviation of the monthly mean values, and the variability in C/N ratio (±1.3).
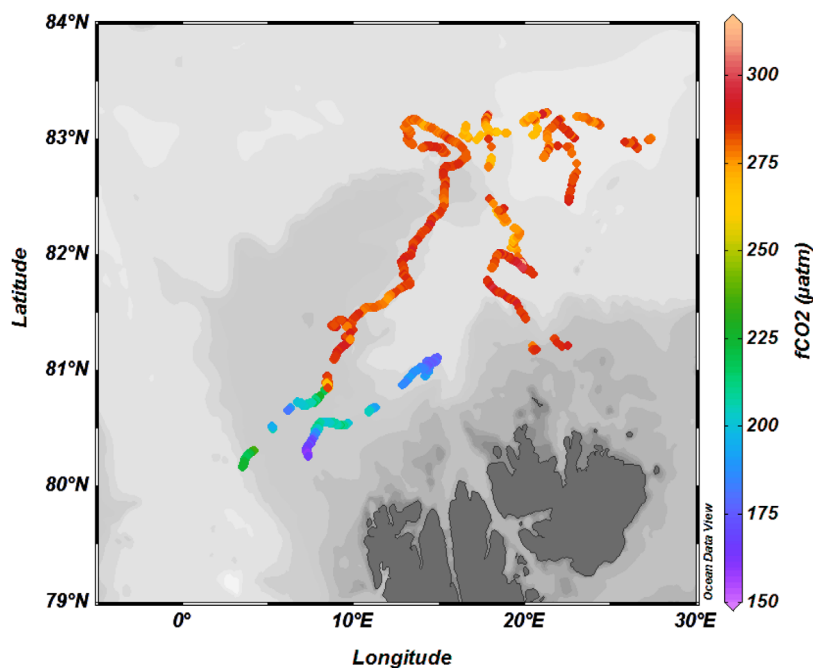
Figure 6. Spatial variability of the observed fugacity of carbon dioxide (fCO_2, µatm) in the upper 5 m for the entire study. Gray-shaded gradients denote bathymetry from dark gray (shallow) to light gray (deep).

4. Results

4.1. Fugacity of Under-Ice Water CO_2

From January to June, fCO_2 ranged between a maximum fCO_2 of 315 µatm (in winter) and a minimum fCO_2 of 153 µatm (in spring) (Figures 6 and 7a–7d and Table 4). Consequently, the surface water was undersaturated relative to the atmospheric fCO_2 level of approximately 400 µatm. The fCO_2 undersaturation ranged between 81 (winter) and 254 µatm (spring) in the deep basin, on the slopes and Yermak Plateau (Table 5). The fCO_2 mean values for Floe 1 and Floe 2 were 283 µatm and showed little variation, as shown in the standard deviations (Table 4). By Floe 3, the mean fCO_2 had decreased to 272 µatm and had larger variability than previous floes. The decrease continued and reached a fCO_2 mean value for Floe 4 of 189 µatm (Table 4). At the end of May, fCO_2 decreased rapidly from winter values to 180 µatm and in June reached the minimum fCO_2 of 153 µatm (Table 4 and Figure 7d). This decrease coincided with an increase of chlorophyll a (Figure 8a) and a nitrate decrease by 10 mmol m^{-3} (Figure 8b) [*Assmy et al.*, 2017].

4.2. Storm Effect on fCO_2 and Response Time

At various occasions, particularly during Floe 1 fCO_2 peaked, coinciding with storm events (Table 3 and Figure 7a). On 5–6 February, the wind increased rapidly from 7.3 to 15 m s^{-1} (storm M2; Figures 2 and 9a). After 15 h, fCO_2 increased by 42 µatm from 270 to 312 µatm (Figure 9a). However, there was only a 3 h lag between the maximum wind speed and the maximum fCO_2 (Figure 9a). After 12 h, fCO_2 returned to 270 µatm. However, the timing of the maximum wind speed and the maximum fCO_2 differed between storm events. During storm event M3, on 13–14 February, the response time was almost 17 h between the maximum wind speed (10 m s^{-1}) and the maximum fCO_2 (315 µatm; Figure 9b).

4.3. Sea-Air CO_2 Fluxes

From winter to spring, the surface-water fCO_2 was undersaturated (ΔfCO_2) relative to the atmospheric fCO_2 levels and was a potential ocean sink of atmospheric CO_2 (Table 5). However, the observed surface-water fCO_2 was under sea ice and could only equilibrate with the atmospheric CO_2 during short periods of openings in leads and cracks in the ice cover. The ΔfCO_2 for each floe was combined with wind speed data and open-water fractions (OW, Table 5) to determine the sea-air CO_2 fluxes using
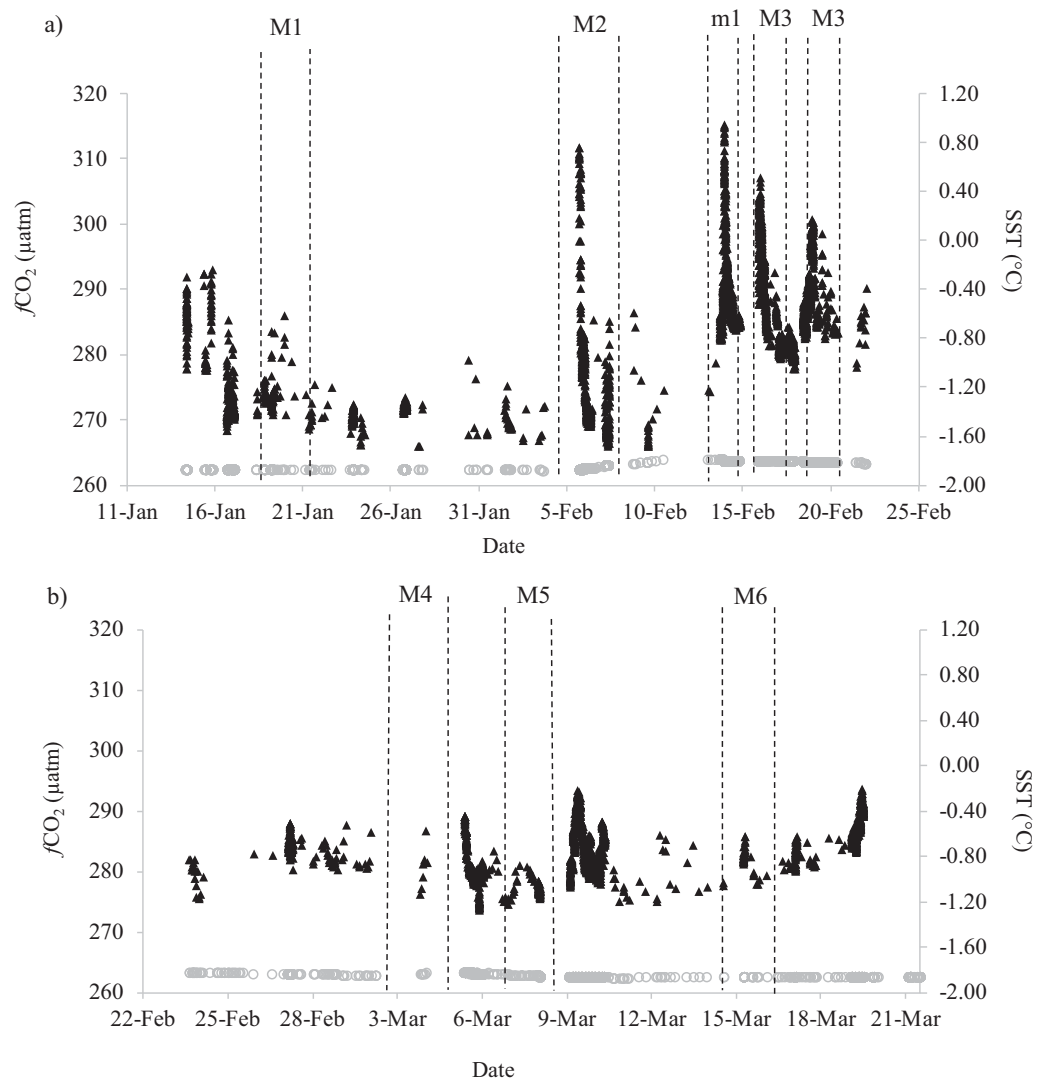
Figure 7. Continuous high-frequency under-ice fCO_2 measurements (fCO_2, μatm; black, filled circles, left y axis) and surface-water temperature (SST, C°; gray, filled circles, right y axis) from January to June for the different floes, where the dotted areas show the major storm events, defined by *Cohen et al.*, [2017], affecting fCO_2; (a) Floe 1, (b) Floe 2, (c) Floe 3, and (d) Floe 4. M1, M2, m1 and M3 are storm events during Floe 1; M4, M5 and M6 are storm events during Floe 2; M7and M8 during Floe 3; and m10 during Floe 4 (Table 3).

equations (4) and (5). The average sea-air CO_2 fluxes were estimated at average wind speed and average OW, and the maximum (minimum) sea-air CO_2 fluxes at maximum (minimum) wind speed (storm event) and maximum OW to evaluate the range of the CO_2 fluxes during the study period (Table 5). Storm events contributed to an increase in fCO_2; hence, the undersaturation decreased to -81 μatm (less negative ΔfCO_2; Table 5). However, the highest wind speeds (23 m s^{-1}) caused a sea-air CO_2 flux of -8 mmol C m^{-2} d^{-1} that was more than 20 times larger than at average wind speed and average ΔfCO_2 in winter (Floe 1 and 2), and about 3 times larger than during spring average flux (Floe 3 and 4). The largest sea-air CO_2 flux of -80 mmol C m^{-2} d^{-1} occurred at high wind speeds (>15 m s^{-1}) combined with the largest undersaturation and largest OW of 53% at Floe 4 (Table 5). At minimum wind speed and maximum undersaturation (most negative ΔfCO_2), the CO_2 fluxes were insignificant (Table 5). The average sea-air CO_2 fluxes using mean wind speed varied between -1.2 and -14 mmol C m^{-2} d^{-1} and were used for comparison with other studies for each floe. Table 6 summarizes the rapid and short-term sea-air CO_2 fluxes during major storm events. During storms with wind speed higher than 19 m s^{-1}, CO_2 sink was larger than 10 mmol m^{-2} d^{-1}, lasting from 12 h to 2 days. Lower wind speed in April caused 50% less CO_2 sink.
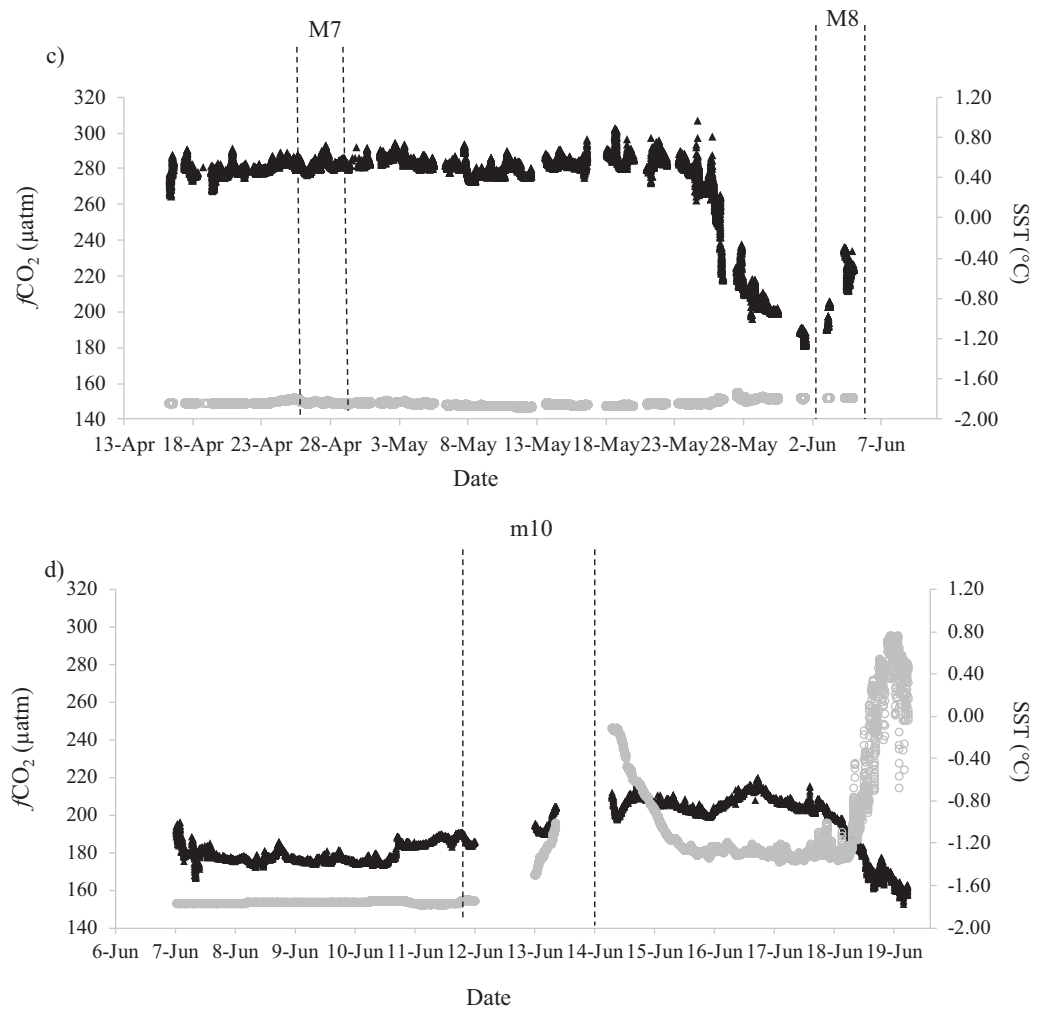
Figure 7. (continued)

Table 5. Sea-Air CO_2 Fluxes (F) at Average Observed fCO_2 (µatm) and at Different fCO_2 and Wind Speed Scenarios (u, m s^{-1}) for Each Floe, "Max" and "Min" Denote Scenarios at Maximum and Minimum Wind Speed (u), Respectively[a]

Floe	fCO_2^{air} (µatm)	ΔfCO_2 (µatm)	u (m s^{-1})		OW (%)	F (mmol C m^{-2} d^{-1} Potential)	F (mmol C m^{-2} d^{-1})	F (mg C m^{-2} d^{-1})
1	396	−113	Average	7.3	2	−16	−0.33	−4
2	399	−116	Average	5.7	3	−10	−0.31	−4
3	408	−136	Average	6.2	4	−14	−0.57	−7
4	407	−218	Average	6.7	12	−26	−3.1	−37
1	396	−81	Max	23	7	−117	−8	−99
2	399	−105	Max	19	11	−105	−14	−164
3	408	−100	Max	15	13	−64	−7	−85
4	407	−188	Max	17	53	−151	−80	−955
1	396	−130	Min	0.2	7	0	0	0
2	399	−125	Min	0.1	11	0	0	0
3	408	−226	Min	0.0	13	0	0	0
4	407	−254	Min	0.7	53	0	−0.2	−2

[a]At minimum wind speed, the estimate is based on maximum ΔfCO_2, and the maximum wind speed at the minimum ΔfCO_2 since fCO_2 generally increased during storm events. Negative ΔfCO_2 means potential for CO_2 flux from atmosphere to water. OW refers to the maximum and average percentage (%) of open water for each floe used in the estimates of the flux. We assumed 100% open water to estimate the potential CO_2 fluxes if no sea ice is present. C in the unit denotes carbon. Negative flux (F) means ocean uptake (or influx) of atmospheric CO_2.
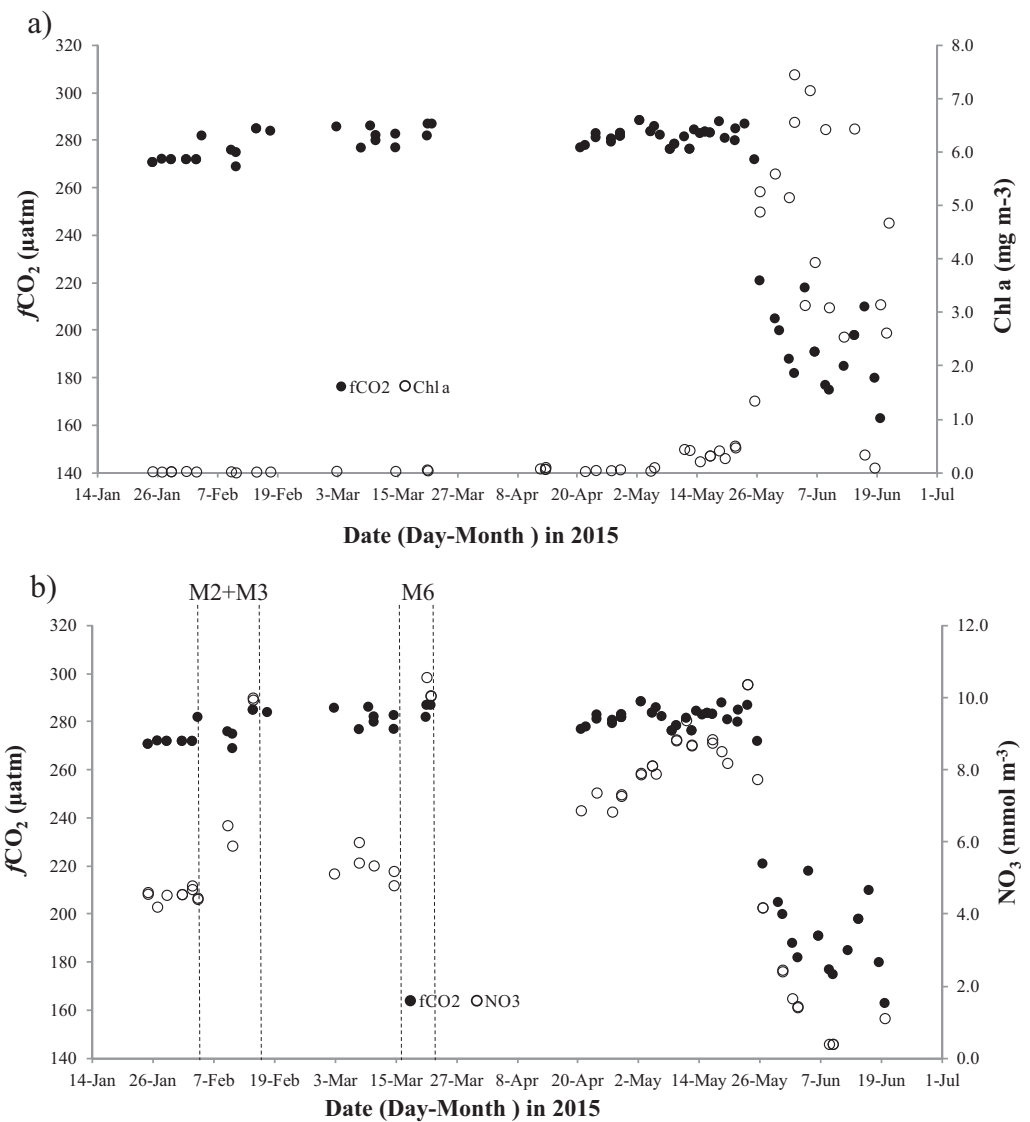
Figure 8. The daily averages of observed fugacity of carbon dioxide (fCO_2, µatm; black, filled circles, left y axis), and the (a) chlorophyll a concentration (Chl a, mg m^{-3}; open circles, right axis,) and (b) nitrate concentration (NO$_3$, mmol m^{-3}; open circles, right axis) from January to June 2015 [*Assmy et al.*, 2016]. M2, M3, and M6 in Figure 6b denote storm events (Table 3) defined by *Cohen et al.*, [2017].

4.4. Drivers Affecting Under-Ice Water fCO_2
4.4.1. Monthly Changes in fCO_2 Drivers

Figure 10a summarizes the monthly change in the observed fCO_2 change (dfCO_{2obs}) from the different biogeochemical drivers. A positive change denotes that the driver has resulted in a fCO_2 gain and a negative change refers to a loss of fCO_2 in the surface waters. Also, included are the uncertainties of the calculations for each driver shown as error bars. The uncertainty was largest in the estimates of $\frac{df\,CO2_{CaCO3}}{dt}$ since that calculation includes all uncertainties from all drivers.

In February, May, and June had the largest observed fCO_2 change (Figure 10a). In February, a net gain in fCO_2 was observed, whereas in May and June the observed fCO_2 showed a net loss (negative). It is evident that biological processes ($\frac{df\,CO2_{bio}}{dt}$) played a major role in June, with a fCO_2 loss of 71 µatm, explained by CO_2 consumption during primary production (Figures 10a and 10b). The effect of vertical mixing ($\frac{df\,CO2_{mix}}{dt}$) was important in February in May, resulting in a fCO_2 gain of 19 and 17 µatm, respectively. This was likely a contribution of CO_2 from subsurface waters to the upper 10 m. Part of this gain was balanced out by the loss in CaCO$_3$ dissolution, particularly in May (–34 µatm). In March and April, the observed fCO_2 changed

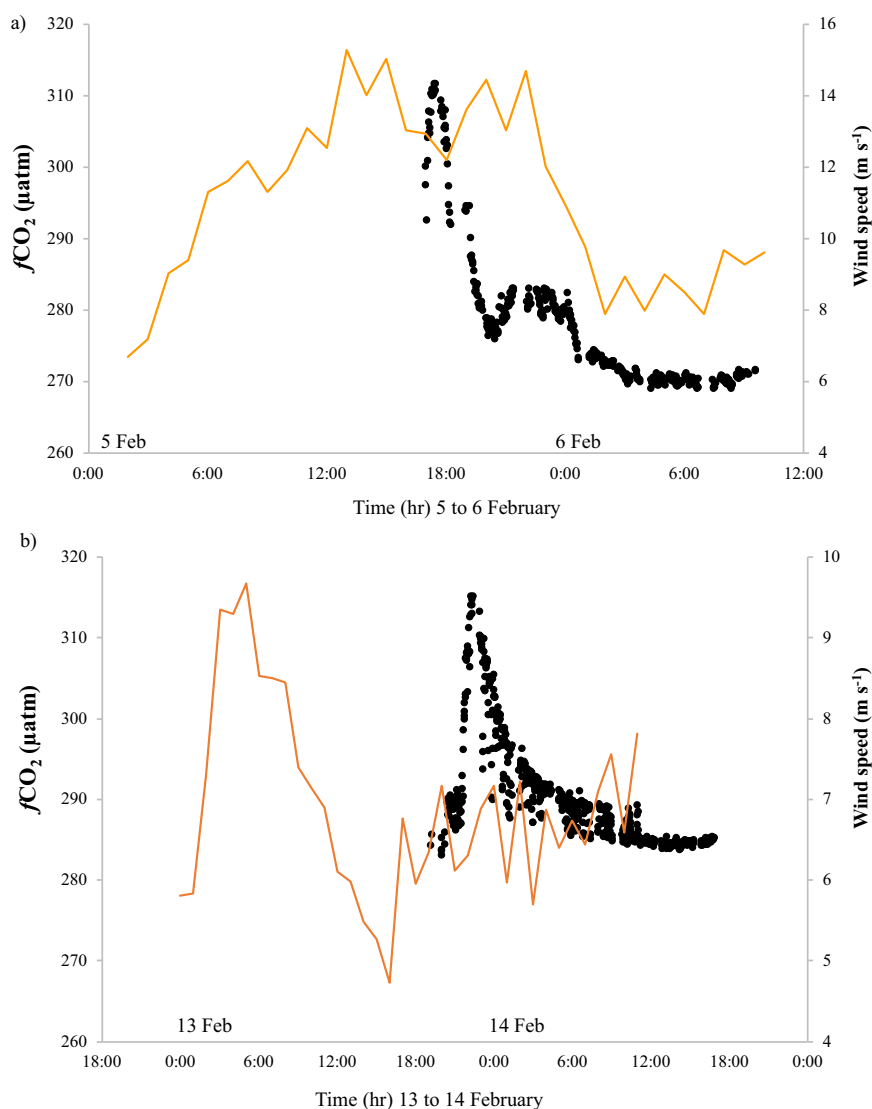**Figure 9.** Under-ice fCO_2 (μatm; left y axis; black, filled circles) and wind speed (u, m s^{-1}; right y axis, orange line) at selected storm events M2 on (a) 5–6 February, and m1 (b) 13 February (Table 3).

insignificantly, and the gain from mixing and the CO_2 flux ($\frac{df\ CO2_{flux}}{dt}$) was balanced by the loss due to $CaCO_3$ dissolution ($\frac{df\ CO2_{CaCO3}}{dt}$). During winter, salinity and temperature were relatively constant (Table 4 and Figures 7a and 7b) and the effects on fCO_2 ($\frac{df\ CO2_S}{dt}$, $\frac{df\ CO2_T}{dt}$) were insignificant (Figure 10a). However, toward the end of the study in spring (in May–June), the salinity effect decreased fCO_2 by approximately 4 μatm. The loss by freshening in June was nearly canceled out by the fCO_2 gain of 6 μatm from warming. The gain in fCO_2 from uptake of CO_2 by sea-air CO_2 flux ($\frac{df\ CO2_{flux}}{dt}$) was 31 μatm (Figure 10a). During the other months, the CO_2 flux contributed to the change in fCO_2 of a small gain of between 2 and 7 μatm (Figure 10a). From this study, we also found that the other major driver explaining the fCO_2 change was the loss of fCO_2 from $CaCO_3$ dissolution, which consumed CO_2 throughout the whole 5 month period (Figure 10a). Between January and April, the effect of $\frac{df\ CO2_{CaCO3}}{dt}$ was the only driver resulting in a loss of fCO_2, varying between 2 μatm (January), 12 μatm (February) and 10 μatm (March). In May and June, this effect resulted in a net loss of 34 and 41 μatm, respectively.

Figure 10b shows the relative contribution of each effect on the total fCO_2 change (absolute sum) during the 5 month period. Biological processes and $CaCO_3$ dissolution were the two major drivers for the total fCO_2 change, contributing 26 and 38%, respectively (Figure 10b). The gain through vertical mixing was large

Table 6. Sea-Air CO_2 Fluxes (F) at Storm Events at Mean ΔfCO_2 (μatm) and at Average and Maximum (Peak) Wind Speed Scenarios (u, m s^{-1}) for Five Storm Events (Table 3)[a]

Date (Day Month)	Floe# (Storm Event)	ΔfCO_2 (μatm)	u (m s^{-1})		OW (%)	F (mmol C m^{-2} d^{-1})	F (mg C m^{-2} d^{-1})
5 Feb	F1 M2	−110	Average	12.2	7	−3.1	−37
6 Feb	F1 M2	−124	Average	9.9	7	−2.3	−28
5 Feb	F1 M2	−110	Peak	22	7	−10	−121
6 Feb	F1 M2	−124	Peak	22	7	−11.5	−137
15 Feb	F1 M3	−97	Average	16.3	7	−4.9	−59
16 Feb	F1 M3	−105	Average	9.9	7	−2.0	−24
17 Feb	F1 M3	−115	Average	7.6	7	−1.3	−15
18 Feb	F1 M3	−107	Average	8.4	7	−1.4	−17
19 Feb	F1 M3	−97	Average	8.4	7	−1.3	−16
15 Feb	F1 M3	−97	Peak	23	7	−9.4	−112
16 Feb	F1 M3	−105	Peak	23	7	−10	−121
17 Feb	F1 M3	−115	Peak	11.9	7	−3.1	−37
18 Feb	F1 M3	−107	Peak	11.9	7	−2.9	−35
19 Feb	F1 M3	−97	Peak	11.9	7	−2.6	−31
15 Mar	F2 M6	−113	Average	12.6	11	−5.4	−64
16 Mar	F2 M6	−114	Average	11.2	11	−4.3	−51
15 Mar	F2 M6	−113	Peak	19.2	11	−12.5	−150
16 Mar	F2 M6	−114	Peak	19.2	11	−12.6	−151
25 Apr	F3 M7	−113	Average	8.0	13	−2.6	−31
26 Apr	F3 M7	−115	Average	9.8	13	−3.9	−47
27 Apr	F3 M7	−111	Average	8.8	13	−3.0	−36
25 Apr	F3 M7	−113	Peak	12.6	13	−6.3	−76
26 Apr	F3 M7	−115	Peak	12.6	13	−6.5	−77
27 Apr	F3 M7	−111	Peak	12.6	13	−6.2	−75
12 Jun	F4 m10	−201	Average	14.1	53	−57	−686
13 Jun	F4 m10	−201	Average	10.8	53	−34	−404
12 Jun	F4 m10	−201	Peak	17.3	53	−86	−1031
13 Jun	F4 m10	−201	Peak	17.3	53	−86	−1031

[a]We used the maximum open-water fraction for the respective floe (OW, %).

in winter and contributed 16% of the total fCO_2 change, and sea-air CO_2 flux contributed 16% of the total fCO_2 change, mainly in June. The salinity and temperature played minor roles in the total change; 2% due to freshening by meltwater and 3% due to warming (Figure 10b).

4.4.2. Effect of Drivers on fCO_2 During Storm Events

We used the same approach to estimate the monthly fCO_2 change described in equations (6–9) to derive the major drivers during one major storm event M2 on 5–6 February (Table 3). Consequently, the increase of 42 μatm in under-ice water fCO_2 was largely caused by the addition of 72 μatm of fCO_2 by mixing of subsurface water. In addition, $CaCO_3$ dissolution resulted in a fCO_2 loss of 31 μatm. The temperature, salinity, and sea-air CO_2 flux had negligible effects.

5. Discussion

5.1. Drivers of Observed fCO_2 and Sea-Air CO_2 Flux Variability

From the study of monthly drivers of the observed fCO_2 change we discovered that biological effects (spring), $CaCO_3$ dissolution (winter and spring), and vertical mixing (winter) had the major impacts on the fCO_2 changes. Here we further investigate these processes to confirm our findings. We found that calculated fCO_2 was >300 μatm at 100 m in the water column based on A_T and DIC values [*Fransson et al.*, 2016], which partly supports our results of increased fCO_2 as a result of vertical mixing of CO_2 with the surface water. It was clear that mixing of subsurface water occurred during winter from observations on salinity and temperature in the upper 10 m. This was particularly active during storm events. For example, *Peterson et al.* [2017] explained a temperature increase at 10 m depth to be caused by vertical mixing of the surface layer. Moreover, *Meyer et al.* [2017a, 2017b] observed deepening of the mixed layer explained by vertical mixing of subsurface water during the storm event on 5–7 February (Figure 2a). In addition, *Koenig et al.* [2016] observed increased salinity in the surface water under the ice during storm events in winter based on IAOOS buoy data. This increase was suggested to be a result of vertical mixing and brine rejection. *Fer et al.*
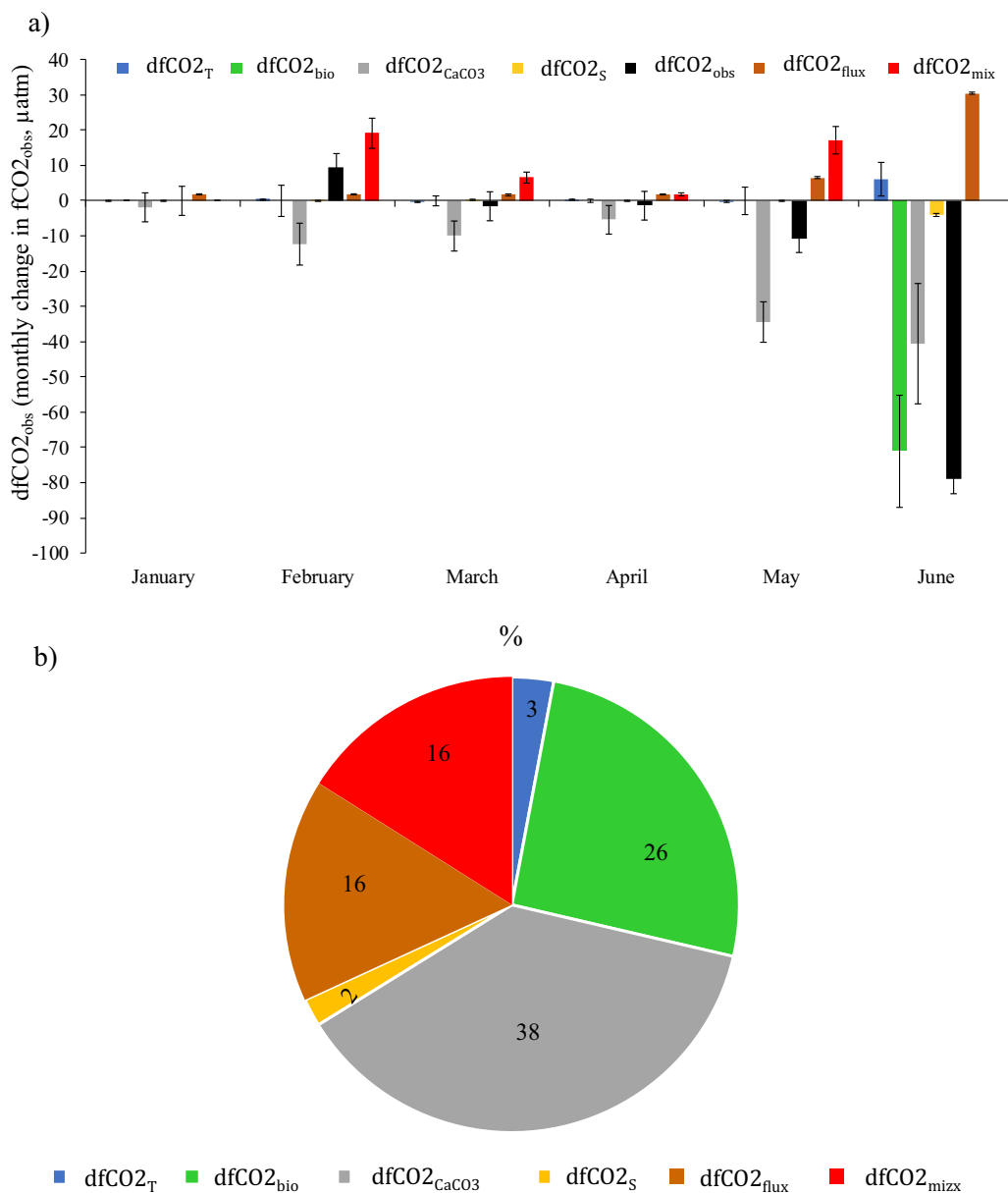
a)

b)

Figure 10. Effects of biogeochemical drivers on surface-water $f\mathrm{CO}_2$ from January to June indicating (a) monthly changes (µatm) in observed $f\mathrm{CO}_2$ ($df\mathrm{CO}_{2obs}$; black) due to surface-water temperature ($df\mathrm{CO}_{2T}$, µatm; blue), salinity ($df\mathrm{CO}_{2S}$; yellow), biological processes ($df\mathrm{CO}_{2bio}$; green), vertical mixing ($df\mathrm{CO}_{2mix}$; red), calcium carbonate precipitation and dissolution ($df\mathrm{CO}_{2CaCO3}$, µatm; gray), and sea-ice CO_2 flux ($df\mathrm{CO}_{2flux}$; orange), and (b) relative change (%) on observed $f\mathrm{CO}_2$ for each biogeochemical driver of surface-water temperature ($df\mathrm{CO}_{2T}$, blue), salinity ($df\mathrm{CO}_{2S}$; yellow), biological processes ($df\mathrm{CO}_{2bio}$; green), vertical mixing ($df\mathrm{CO}_{2mix}$; red), calcium carbonate (CaCO_3) precipitation and dissolution ($df\mathrm{CO}_{2CaCO3}$; gray), and sea-ice CO_2 flux ($df\mathrm{CO}_{2flux}$; orange).

[2017] investigated the proportions of vertical mixing and brine contribution to salinity in winter to be 90 and 10%, respectively.

Interestingly, the effect on the $f\mathrm{CO}_2$ change due to CaCO_3 dissolution was prominent throughout the study and larger than the biological effect (Figures 10a and 10b). In our calculations, this effect was derived from the residual of the sum of all other drivers and the observed $f\mathrm{CO}_2$ change. Consequently, this term has the largest uncertainty and it is useful to consider another independent calculation method to investigate the magnitude to this effect. *Fransson et al.* [2013] used A_T and salinity ratio (AT/S) in under-ice water to estimate CaCO_3 (ikaite) dissolution. In our study, the AT/S in seawater was 66 from the water below 50 m

[*Fransson et al.*, 2016] and 69 from under-ice water (upper 5 m). This enhanced AT/S under the ice supported $CaCO_3$ dissolution in the under-ice water [*Fransson et al.*, 2016]. The maximum AT/S increase was converted to a dissolution of $CaCO_3$ of 74 μmol kg^{-1}, corresponding to a DIC change of 37 μmol kg^{-1} (74/2; equation (1)). From the driver estimates in this study, $CaCO_3$ dissolution decreased fCO$_2$ by 34 μatm in May and a maximum of 41 μatm in June (Figure 10a). This corresponds to a DIC change of 19 and 36 μmol kg^{-1}, respectively. This comparison of the two methods supports the finding that $CaCO_3$ dissolution was an important driver for the fCO$_2$ loss during our study. The total loss of fCO$_2$ due to $CaCO_3$ dissolution corresponds to 0.7 mol m^{-2} in the upper 10 m. Our findings are also supported by the results from a study in Arctic sea ice by *Rysgaard et al.* [2013], where they estimated higher ikaite concentrations (100–200 μmol kg^{-2}) than our results using another method on nonmelted sea ice at the ice-water interface. These values are considered comparable to our results of 64 μmol kg^{-1} as the sum of ikaite dissolution for the entire study. *Geilfus et al.* [2016] estimated the effect of ikaite dissolution of 64–66 μmol kg^{-1} in an experimental mesocosm in an outdoor pool in Greenland.

Our study supports previous findings that dissolution of $CaCO_3$ contributes to sustaining the relatively low surface-water fCO$_2$ values and undersaturation (with regard to atmospheric CO_2 levels) in the surface water in winter in polar oceans, as also suggested by *Rysgaard et al.* [2012] and *Geilfus et al.* [2016].

The pronounced loss of fCO$_2$ due to biological processes at the end of May and June coincided with an extensive under-ice phytoplankton bloom dominated by the haptophyte algae *Phaeocystis pouchetii* observed by *Assmy et al.* [2017] at the same location. This supports our finding that a large part of the fCO$_2$ decrease was explained by biological CO_2 drawdown. Recalculating our results of biological effect in the upper 50 m, we obtain values of approximately 1.6 mol m^{-2}, which is similar to a study by *Assmy et al.* [2017] of 1.3 mol m^{-2} using another method in the same area, and lower than the result of 2.6 mol m^{-2} in a study by *Fransson et al.* [2001], in the Barents Sea. However, the Arctic Ocean has large regional differences in shelf areas and deep ocean entailing river runoff and variable conditions for primary production [e.g., *Carmack et al.*, 2006].

Except for June, the surface ocean was more than 90% ice-covered. This implies that surface-water fCO$_2$ could only equilibrate with the atmospheric CO_2 during short periods of openings in leads and cracks in the ice cover. The relatively large surface-water fCO$_2$ undersaturation due to primary production increased the potential for CO_2 uptake from the atmosphere, in combination with more open water. In spring, Floe 4 had the largest ΔfCO$_2$, which resulted in the largest sea-air CO_2 flux at average and maximum wind speed. However, scenarios with the lowest wind speed resulted in insignificant CO_2 flux, suggesting that strong wind, even in winter, with more ice cover, was as important as large ΔfCO$_2$ for driving the sea-ice CO_2 fluxes. This result is supported by a previous sea-air CO_2-flux study by *Fransson et al.* [2004] which found that the fluctuations in wind speed showed a larger impact on the variability of the fluxes than the fluctuations in ΔfCO$_2$. In spring, surface-water temperature increased and salinity decreased due to bottom ice melt [*Meyer et al.*, 2017a, 2017b]. Studies by *Rysgaard et al.* [2012] and *Fransson et al.* [2013] showed that $CaCO_3$ dissolution increased the potential for atmospheric CO_2 uptake by the surface ocean during ice melt by 10.5 mmol m^{-2} ice d^{-1} and 50 mmol m^{-2} d^{-1}, respectively. This process, in combination with primary production and open water, contributes to the large fCO$_2$ undersaturation and sea-air CO_2 flux in spring.

5.2. Sea-Air CO$_2$ Fluxes Comparison in the Arctic Ocean

The sea-air CO_2 fluxes using average wind speed and average OW for each floe were compared to a scenario an ice-free ocean (100% OW), referred as the potential CO_2 flux (Table 5). The potential sea-air CO_2 fluxes using average wind speed were between −10 and −26 mmol C m^{-2} d^{-1} (Table 5) and 8–48 times higher than average sea-air CO_2 fluxes (–0.3 to −3.1 mmol m^{-2} d^{-1}). However, during storm events with maximum wind speed varying between 15 and 23 m s^{-1}, and with the estimated potential sea-air CO_2 fluxes at 100% OW, the fluxes largely increased (Table 5).

The first high-frequency fCO$_2$ measurements under the sea ice, and estimates of sea-air CO_2 fluxes, were carried out in the Canadian Arctic Archipelago (CAA) by *Fransson et al.* [2009]. They estimated that sea-air CO_2 fluxes varied between −50 mmol C m^{-2} d^{-1} (CO_2 sink) and 18 mmol C m^{-2} d^{-1} (CO_2 source) in open water (OW) in summer 2005. In the ice-covered part of the CAA, the surface water was a CO_2 sink of about −6 mmol m^{-2} d^{-1} [*Fransson et al.*, 2009]. They found that CO_2 fluxes were affected by freshwater from river runoff and sea-ice melt as well as upwelling and primary production. *Else et al.* [2012] did seasonal studies

in the CAA and in the upwelling region off Cape Bathurst and estimated CO_2 fluxes between -10 and 6.5 mmol C m^{-2} d^{-1}. These values are similar to our study for the average total CO_2 fluxes (100% OW) of between -10 and -26 mmol C m^{-2} d^{-1}.

Studies using calculated fCO$_2$ from A$_T$ and DIC, such as *Bates et al.* [2006], estimated winter-time average CO_2 fluxes of -1 to -3 mmol C m^{-2} d^{-1} (i.e., influx of <3 mmol C m^{-2} d^{-1}) in the Central Arctic basin, based on 1% OW. These estimates are slightly larger than our winter-time CO_2 fluxes in February (Floe 1), which was less than -0.3 mmol m^{-2} d^{-1} at average wind speed and OW (as determined for Floe 1 and 2 using average fraction of OW). However, during storm events at peak wind speed, the average sea-air CO_2 flux at maximum wind speed was -10 mmol m^{-2} d^{-1} (Floe 1) and -17 mmol m^{-2} d^{-1} (Floe 2). Extrapolated flux estimates reported by *Yasunaka et al.* [2016] for the Barents Sea, the Chukchi Sea, and an average for the whole Arctic Ocean found the strongest sea-air CO_2 flux (i.e., ocean CO_2 influx) of approximately -12 mmol m^{-2} d^{-1} occurred in winter in the ice-free regions of the Barents Sea (due to storm events). The summer CO_2 influxes were highest in the Chukchi Sea in summer of -10 mmol m^{-2} d^{-1}. The average for the whole Arctic Ocean was -4 mmol m^{-2} d^{-1}. Our estimates at 100% OW, but recalculated using the transfer formulation of *Wanninkhof* [1992] to be consistent with *Yasunaka et al.* [2016], resulted in a potential winter-time (100% OW) sea-air CO_2 flux of between -12 and -20 mmol m^{-2} d^{-1}. This is similar to the magnitude determined for the ice-free waters in the Barents Sea in winter by *Yasunaka et al.* [2016]. In spring and summer our total CO_2 flux at 100% OW and mean wind speed ranged between -17 and -32 mmol C m^{-2} d^{-1} (Floe 3 and Floe 4). These estimates are larger than the CO_2 flux of -10 mmol C m^{-2} d^{-1} estimated by *Yasunaka et al.* [2016] in summer.

Our average sea-air CO_2 fluxes (average OW and wind speed) in spring (Floe 3 and 4) were similar to the estimated fluxes in ice-covered areas in Arctic summer [*Bates et al.*, 2006; *Fransson et al.*, 2009]. In winter (Floe 1 and 2), the average fluxes were less than previously reported values due to extensive sea-ice cover. However, at storm events in ice-covered winter conditions, the maximum sea-air CO_2 flux was in the same order of magnitude or larger than the CO_2 fluxes in ice-free regions as the Barents Sea and Chukchi Sea [*Fransson et al.*, 2009; *Yasunaka et al.*, 2016]. This result means that the openings in the ice cover due to storm events were highly efficient as promotor for CO_2 exchange, even in winter.

5.3. Sea-Air CO$_2$ Fluxes Comparison in the Antarctic Ocean

In contradiction to the mixture of MYI and FYI ice in the Arctic Ocean, the Antarctic Ocean (or Southern Ocean) consists mostly of seasonal FYI, which forms and melts every year. With climate change, less ice cover, thinning of ice, and more FYI in the Arctic Ocean, a comparison between the two oceans is highly relevant.

Mu et al. [2014] used measured fCO$_2$ to estimate sea-air CO_2 fluxes in the Amundsen Sea (Antarctica) and found a large net sink for atmospheric CO_2 (with a spatially averaged flux density) of -18 ± 14 mmol C m^{-2} d^{-1}. This high flux suggested a large influence on the uptake of CO_2 by the Antarctic Ocean. Our average CO_2-flux estimates varying between -1.2 and -14 mmol m^{-2} d^{-1} (Table 5) are within the range of flux estimates by *Mu et al.* [2014]. The Amundsen Sea region has experienced a significant increase in open-water duration (1979–2013), and *Mu et al.* [2014] discuss whether this CO_2 sink will increase with future climate-driven change. The central region revealed a high CO_2 flux of -36 ± 8.4 mmol C m^{-2} d^{-1}, which was approximately 50% larger than that reported for the peak of the bloom in the Ross Sea (Antarctica), comparable to high rates reported for the Chukchi Sea (Arctic Ocean) [*Mu et al.*, 2014]. *Chierici et al.* [2012] projected a potential for CO_2 uptake in the open-water area north of the Amundsen Sea and in the Ross Sea in austral summer due to the large fCO$_2$ undersaturation of about -150 μatm in the Ross Sea. This undersaturation was similar to the estimates by *Bates et al.* [1998] in the Ross Sea polynya where they used calculated fCO$_2$ from A$_T$ and DIC to estimate sea-air CO_2 fluxes of -10 mmol CO$_2$ m^{-2} d^{-1}. By calculating fCO$_2$ from A$_T$ and DIC, *Metzl et al.* [2006] estimated sea-air CO_2 fluxes of -1 to -4 mmol C m^{-2} d^{-1} in the seasonal ice zone (SIZ) south of 58°S in the Antarctic Ocean during the open season in austral summer. *Chierici et al.* [2004] estimated sea-air CO_2 fluxes which ranged between -20 (CO$_2$ sink) and 1.3 (CO$_2$ source) mmol m^{-2} d^{-1} with an average of -3 mmol m^{-2} d^{-1} from the polar front to the continent in the Atlantic sector of the Antarctic Ocean. In that region, the largest ocean CO_2 uptake (sink) was estimated at the polar front [*Chierici et al.*, 2004].

There are few previous estimates of sea-air CO_2 fluxes in winter in Antarctica. Our wintertime average CO_2-fluxes (average wind speed and OW) were lower compared to the estimates in the SIZ (seasonal ice zone) of the Antarctic Ocean [*Metzl et al.*, 2006]. However, at storm events in winter, our fluxes were within the

range of CO_2 fluxes estimated by other studies in the open parts of the Antarctic Ocean [*Bates et al.*, 1998; *Chierici et al.*, 2004; *Metzl et al.*, 2006; *Mu et al.* 2014]. Our results indicate that openings and lead in the ice cover in winter during storm events were as important for the ocean CO_2 uptake as in the seasonally ice-free oceans in summer in Antarctica. This result implies an increased potential of ocean CO_2 uptake in the Arctic Ocean in a future climate, similar to the open water in the Antarctic Ocean.

6. Conclusion

During the N-ICE2015 expedition north of Svalbard [*Granskog et al.*, 2016], we explored an area in the Arctic Ocean where no winter-time surface-water fCO_2 under the ice has previously been measured. From this unique data set obtained from January to June, we followed the changes in the underlying water (upper 10 m) fCO_2, drivers and sea-air CO_2 fluxes. The effect of dissolution of $CaCO_3$ (e.g., ikaite) decreased under-ice water fCO_2 during the entire study, and biological CO_2 uptake was the main cause of fCO_2 drawdown in spring. We found substantial peaks in fCO_2 coinciding with storm events, which induced more ocean mixing of CO_2. Storm events caused rapid warming in air and water [*Peterson et al.*, 2017; *Cohen et al.*, 2017], and opening of leads, that resulted in substantial and short-term increase in the underlying fCO_2, facilitating ocean CO_2 uptake. Increased air temperature has been shown to increase the sea-ice brine volume and permeability of the ice [e.g., *Cox and Weeks*, 1983], creating pulses of CO_2-rich brine or $CaCO_3$ rejected from the ice to underlying water. Consumption of CO_2 based on $CaCO_3$ dissolution sustained undersaturation of fCO_2, which is supported by previous findings [*Rysgaard et al.*, 2013; *Geilfus et al.*, 2016]. By June, the CO_2 loss due to primary production confirmed by *Assmy et al.* [2017] further enhanced the fCO_2 undersaturation relative to the atmospheric CO_2 level. At that time, we estimated the largest oceanic CO_2 sink (influx) of atmospheric CO_2. This was a result of the combined conditions of the largest ΔfCO_2 (largest undersaturation due to the bloom), relatively high wind speeds and open water of up to 53%. In a scenario of a change from a perennial MYI to seasonal and warmer FYI in combination with more openings in the Arctic sea-ice pack, such as leads and cracks, will facilitate additional gas exchange between the atmosphere and the Arctic Ocean. Increased storm activity would also increase addition of CO_2 from subsurface waters due to vertical mixing, hence decreasing the fCO_2 undersaturation. In addition, it is likely that the combination of more open water and high wind speeds will result in increased CO_2 flux (ocean uptake). Perhaps also occasionally, net outgassing of CO_2 would occur, as has been observed in the wind-induced upwelling areas of the southern Bering Sea [*Fransson et al.*, 2006] and the Canadian Arctic Archipelago [e.g., *Fransson et al.*, 2009; *Else et al.*, 2012]. The Arctic Ocean might perhaps become more similar to the Antarctic Ocean, so-called "Antarctification," with more seasonal FYI and less MYI over the deep basins, and increased open-water exposure to sea-air CO_2 exchange in summer. However, the direction of the net CO_2 flux in the Arctic Ocean water-ice-air system needs further investigation.

References

Assmy, P., et al. (2016), N-ICE2015 Water Column Biogeochemistry, Norw. Polar Inst., Tromsø, Norway, doi:10.21334/npolar.2016.3ebb7f64.

Assmy, P., et al. (2017), Leads in Arctic pack ice enable early phytoplankton blooms below snow covered sea ice, *Sci. Rep.*, 7, 40850, doi: 10.1038/srep40850.

Assur, A. (1960), Composition of sea ice and its tensile strength, *U.S. Army Snow Ice Permafrost Res. Estab. Res. Rep. 44*, Corps of Eng., Wilmette, Ill.

Bakker, D. C. E., et al. (2016), A multi-decade record of high-quality fCO_2 data in version 3 of the surface ocean CO_2 atlas (SOCAT), *Earth Syst. Sci. Data*, 8, 383–413, doi:10.5194/essd-2016-15.

Bates, N. R., D. A. Hansell, and C. A. Carlson (1998), Distribution of CO_2 species, estimates community production, and air-sea exchange in the Ross Sea Polynya, *J. Geophys. Res.*, 103(C2), 2883–2896.

Bates, N. R., and J. T. Mathis (2009), The Arctic Ocean marine carbon cycle: Evaluation of air-sea CO_2 exchanges, ocean acidification impacts and potential feedbacks, *Biogeosciences*, 6, 2433–2459.

Bates, N. R., S. B. Moran, D. A. Hansell, and J. T. Mathis (2006), An increasing CO_2 sink in the Arctic Ocean due to sea-ice loss, *Geophys. Res. Lett.*, 33, L23609, doi:10.1029/2006GL027028.

Bendschneider, K., and R. I. Robinson (1952), A new spectrophotometric method for the determination of nitrite in seawater, *J. Mar. Res.*, 2, 87–96.

Carmack, E., D. Barber, J. Christensen, R. Macdonald, B. Rudels, and E. Sakshaug (2006), Climate variability and physical forcing of the food webs and the carbon budget on panarctic shelves, *Prog. Oceanogr.*, 71, 145–181.

Chierici, M., A. Fransson, D. Turner, E. A. Pakhomov, and P. W. Froneman (2004), Variability in pH, fCO_2, oxygen and flux of CO_2 in the surface water in the Atlantic sector of the Southern Ocean, *Deep Sea Res., Part II*, 51, 2773–2787, doi:10.1016/j.dsr2.2001.03.002.

Chierici, M., A. Fransson, and Y. Nojiri (2006), Biogeochemical processes as drivers of surface fCO_2 in contrasting provinces in the subarctic North Pacific Ocean, *Global Biogeochem. Cycles*, 20, GB1009, doi:10.1029/2004GB002356.

Chierici, M., A. Fransson, B. Lansard, L. A. Miller, A. Mucci, E. Shadwick, H. Thomas, J.-E. Tremblay, and T. Papakyriakou (2011), The impact of biogeochemical processes and environmental factors on the calcium carbonate saturation state in the Circumpolar Flaw Lead in the Amundsen Gulf, Arctic Ocean, *J. Geophys. Res.*, 116, C00G09, doi:10.1029/2011JC007184.

Chierici, M., M. Mattsdotter, S. Signorini, A. Fransson, and A. Olsen (2012), Surface water fCO$_2$ algorithms for the high-latitude Pacific sector of the Southern Ocean, *Remote Sens. Environ.*, 119, 184–196.

Cohen, L., et al. (2017), Meteorological conditions in a thinner Arctic sea ice regime from winter through spring during the Norwegian young sea ICE expedition (N-ICE2015), *J. Geophys. Res. Atmos.*, 122, doi:10.1002/2016JD026034, in press.

Cox, G. F. N., and W. F. Weeks (1983), Equations for determining the gas and brine volumes in sea-ice samples, *J. Glaciol.*, 29, 306–316.

Delille, B., et al. (2014), Southern Ocean CO$_2$ sink: The contribution of the sea ice, *J. Geophys. Res. Oceans*, 119, 6340–6355, doi:10.1002/2014JC009941.

Dickson, A. G. (1990), Standard potential of the (AgCl(s) + 1/2H$_2$ (g) = Ag(s) + HCl(aq)) cell and the dissociation constant of bisulfate ion in synthetic sea water from 273.15 to 318.15 K, *J. Chem. Thermodyn.*, 22, 113–127.

Dickson, A. G., and F. J. Millero (1987), A comparison of the equilibrium constants for the dissociation of carbonic acid in seawater media, *Deep Sea Res., Part A*, 34, 1733–1743.

Dickson, A. G., C. L. Sabine, and J. R. Christian (2007), Guide to best practices for ocean CO$_2$ measurements, *PICES Spec. Publ.*, 3, 191 pp.

Dieckmann, G. S., G. Nehrke, S. Papadimitriou, J. Göttlicher, R. Steininger, H. Kennedy, D. Wolf-Gladrow, and D. N. Thomas (2008), Calcium carbonate as ikaite crystals in Antarctic sea ice, *Geophys. Res. Lett.*, 25, L08501, doi:10.1029/2008GL033540.

Dieckmann, G. S., G. Nehrke, C. Uhlig, J. Göttlicher, S. Gerland, M. A. Granskog, and D. N. Thomas (2010), Brief communication: Ikaite (CaCO$_3$·6H$_2$O) found in Arctic sea ice, *Cryosphere*, 4, 227–230.

Dodd, P., et al. (2016), N-ICE2015 Ship-Based Conductivity-Temperature-Depth (CTD) Data, Norw. Polar Inst., Tromsø, Norway, doi:10.21334/npolar.2017.92262a9c.

Else, B. G. T., T. N. Papakyriakou, R. J. Galley, A. Mucci, M. Gosselin, L. A. Miller, E. H. Shadwick, and H. Thomas (2012), Annual cycles of pCO$_2$sw in the southeastern Beaufort Sea: New understandings of air-sea CO$_2$ exchange in arctic polynya regions, *J. Geophys. Res.*, 117, C00G13, doi:10.1029/2011JC007346.

Else, B. G. T., R. J. Galley, B. Lansard, D. G. Barber, K. Brown, L. A. Miller, A. Mucci, T. N. Papakyriakou, J.-E. Tremblay, and S. Rysgaard (2013), Further observations of a decreasing atmospheric CO$_2$ uptake capacity in the Canada Basin (Arctic Ocean) due to sea ice loss, *Geophys. Res. Lett.*, 40, 1132–1137, doi:10.1002/grl.50268.

Fer, I., A. Peterson, A. Randelhoff, and A. Meyer (2017), One-dimensional evolution of the upper water column in the Atlantic sector of the Arctic Ocean in winter, *J. Geophys. Res. Oceans*, 122, 1665–1682, doi:10.1002/2016JC012431.

Fransson, A., M. Chierici, L. G. Anderson, I. Bussman, E. P. Jones, and J. H. Swift (2001), The importance of shelf processes for the modification of chemical constituents in the waters of the eastern Arctic Ocean: Implication for carbon fluxes, *Cont. Shelf Res.*, 21, 225–242.

Fransson, A., M. Chierici, and L. G. Anderson (2004), Diurnal variations in the oceanic carbon dioxide system and oxygen in the surface water in the Southern Ocean, *Deep Sea Res., Part II*, 51, 2827–2839.

Fransson, A., M. Chierici, and Y. Nojiri (2006), Increased net CO$_2$ outgassing in the upwelling region of the southern Bering Sea in a period of variable marine climate between 1995 and 2001, *J. Geophys. Res.*, 111, C08008, doi:10.1029/2004JC002759.

Fransson, A., M. Chierici, and Y. Nojiri (2009), New insights into the spatial variability of the surface water carbon dioxide in varying sea ice conditions in the Arctic Ocean, *Cont. Shelf Res.*, 29, 1317–1328, doi:10.1016/j.csr.2009.03.008.

Fransson, A., M. Chierici, L. A. Miller, G. Carnat, H. Thomas, E. Shadwick, S. Pineault, and T. M. Papakyriakou (2013), Impact of sea ice processes on the carbonate system and ocean acidification state at the ice-water interface of the Amundsen Gulf, Arctic Ocean, *J. Geophys. Res. Oceans*, 118, 7001–7023, doi:10.1002/2013JC009164.

Fransson, A., et al. (2016), Winter-to-spring evolution of Arctic Ocean acidification state in under-ice water and effect of sea-ice dynamics during N-ICE 2015 ice drift project, paper presented at 4th International Symposium on the OA Ocean in High CO$_2$ World, Hobart, Australia.

Geilfus, N.-X., G. Carnat, T. Papakyriakou, J.-L. Tison, B. Else, H. Thomas, E. Shadwick, and B. Delille (2012), Dynamics of pCO$_2$ and related air–ice CO$_2$ fluxes in the Arctic coastal zone (Amundsen Gulf, Beaufort Sea), *J. Geophys. Res.*, 117, C00G10, doi:10.1029/2011JC007118.

Geilfus, N.-X., R. J. Galley, B. G. T. Else, K. Campbell, T. Papakyriakou, O. Crabeck, M. Lemes, B. Delille, and S. Rysgaard (2016), Estimates of ikaite export from sea ice to the underlying seawater in a sea ice–seawater mesocosm, *Cryosphere*, 10, 2173–2189, doi:10.5194/tc-10-2173-2016.

Golden, K. M., S. F. Ackley, and V. I. Lytle (1998), The percolation phase transition in sea ice, *Science*, 282, 2238–2241.

Golden, K. M., et al. (2007), Thermal evolution of permeability and microstructure in sea ice, *Geophys. Res. Lett.*, 34, L16501, doi:10.1029/2007GL030447.

Granskog, M. A., P. Assmy, S. Gerland, G. Spreen, H. Steen, and L. H. Smedsrud (2016), Arctic research on thin ice: Consequences of Arctic sea ice loss, *Eos Trans. AGU*, 97(5), 22–26, doi:10.1029/2016EO044097.

Granskog, M. A., A. Rösel, P. A. Dodd, D. Divine, S. Gerland, T. Martma, and M. J. Leng (2017), Snow contribution to first-year and second-year Arctic sea ice mass balance north of Svalbard, *J. Geophys. Res. Oceans*, 122, 2539–2549, doi:10.1002/2016JC012398.

Holm-Hansen, O., and B. Riemann (1978), Chlorophyll a determination: Improvements in methodology, *Oikos*, 30(3), 438–447.

Hudson, S., L. Cohen, and V. P. Walden (2015), N-ICE2015 Surface Meteorology v2, Norw. Polar Inst., Tromsø, Norway, doi:10.21334/npolar.2015.056a61d1.

Koenig, Z., C. Provost, N. Villacieros-Robineau, N. Sennéchael, and A. Meyer (2016), Winter ocean-ice interactions under thin sea ice observed by IAOOS platforms during NICE2015: Salty surface mixed layer and active basal melt, *J. Geophys. Res. Oceans*, 121, 7989–7916, doi:10.1002/2016JC012195.

Le Quéré, C., et al. (2015), Global carbon budget 2015, *Earth Syst. Sci. Data*, 7, 349–396.

Lindsay, R., and A. Schweiger (2015), Arctic sea ice thickness loss determined using subsurface, aircraft, and satellite observations, *Cryosphere*, 9(1), 269–283, doi:10.5194/tc-9-269-2015.

Masson, D., and P. H. LeBlond (1989), Spectral evolution of wind–generated surface gravity waves in a dispersed ice field, *J. Fluid Mech.*, 202, 43–81.

McDougall, T. J., D. R. Jackett, F. J. Millero, R. Pawlowicz, and P. M. Barker (2012), A global algorithm for estimating absolute salinity, *Ocean Sci.*, 8(6), 1123–1134.

McPhee, M. G. (2005), Turbulent heat flux in the upper ocean under sea ice, *J. Geophys. Res.*, 97, 5365–5379, doi:10.1029/92JC00239.

Mehrbach, C., C. H. Culberson, J. E. Hawley, and R. M. Pytkowicz (1973), Measurement of the apparent dissociation constants of carbonic acid in seawater at atmospheric pressure, *Limnol. Oceanogr.*, 18, 897–907, doi:10.4319/lo.1973.18.6.0897.

Meier, W. N., et al. (2014), Arctic sea ice in transformation: A review of recent observed changes and impacts on biology and human activity, *Rev. Geophys.*, *52*, 185–217, doi:10.1002/2013RG000431.

Metzl, N., C. Brunet, A. Jabaud-Jan, A. Poisson, and B. Schauer (2006), Summer and winter air-sea CO_2 fluxes in the Southern Ocean, *Deep Sea Res., Part I*, *53*, 1548–1563.

Meyer, A., et al. (2016), N-ICE2015 Ocean Microstructure Profiles (MSS90L), Norw. Polar Inst., Tromsø, Norway, doi:10.21334/npolar.2016.774bf6ab.

Meyer, A., et al. (2017a), Winter to summer hydrographic and current observations in the Arctic north of Svalbard, *J. Geophys. Res. Oceans*, doi:10.1002/2016JC012391, in press.

Meyer, A., I. Fer, A. Sundfjord, and A. K. Peterson (2017b), Mixing rates and vertical heat fluxes north of Svalbard from Arctic winter to spring, *J. Geophys. Res. Oceans*, *122*, doi:10.1002/2016JC012441, in press.

Miller, L. A., T. N. Papakyriakou, R. E. Collins, J. W. Deming, J. K. Ehn, R. W. Macdonald, A. Mucci, O. Owens, M. Raudsepp, and N. Sutherland (2011), Carbon dynamics in sea ice: A winter flux time series, *J. Geophys. Res.*, *116*, C02028, doi:10.1029/2009JC006058.

Mu, L., S. E. Stammerjohn, K. E. Lowry, and P. L. Yager (2014), Spatial variability of surface pCO_2 and air-sea CO_2 flux in the Amundsen Sea Polynya, Antarctica, *Elementa Sci. Anthropocene*, *2*, 000036, doi: 10.12952/journal.elementa.000036.

Nedashkovsky, A. P., S. V. Khvedynich, and T. V. Petovsky (2009), Alkalinity of sea ice in the high-latitudinal arctic according to the surveys performed at north pole drifting station 34 and characterization of the role of the arctic in the CO_2 exchange, *Mar. Chem.*, *49*, 55–63, doi:10.1134/s000143700901007x.

Nomura, D., H. Eicken, R. Gradinger, and K. Shirasawa (2010), Rapid physically driven inversion of the air-sea ice CO_2 flux in the seasonal landfast ice off Barrow, Alaska after onset of surface melt, *Cont. Shelf Res.*, *30*, 1998–2004, doi:10.1016/j.csr.2010.09.014.

Nomura, D., M. A. Granskog, P. Assmy, D. Simizu, and G. Hashida (2013), Arctic and Antarctic sea ice acts as a sink for atmospheric CO_2 during periods of snow melt and surface flooding, *J. Geophys. Res. Oceans*, *118*, 6511–6524, doi:10.1002/2013JC009048.

Notz, D., and M. G. Worster (2009), Desalination processes of sea ice revisited, *J. Geophys. Res.*, *114*, C05006, doi:10.1029/2008JC004885.

Omar, A. M., T. Johannessen, R. Bellerby, A. Olsen, S. Kaltin, C. Kivimae, and L. G. Anderson (2005) Sea ice and brine formation in Storfjorden: Implications for the Arctic wintertime air-sea CO_2 flux, in *The Nordic Seas: An Integrated Perspective, Geophys. Monogr.*, vol. 158, edited by H. Drange et al., pp. 177–188, AGU, Washington, D. C.

Papadimitriou, S., H. Kennedy, G. Kattner, G. S. Dieckman, and D. N. Thomas (2004), Experimental evidence for carbonate precipitation and CO_2 degassing during sea ice formation, *Geochim. Cosmochim. Acta*, *68*, 1749–1761.

Peterson, A. K., I. Fer, M. G. McPhee, and A. Randelhoff (2017), Turbulent heat and momentum fluxes in the upper ocean under Arctic sea ice, *J. Geophys. Res. Oceans*, *122*, 1439–1456, doi:10.1002/2016JC012283.

Pierrot, D., E. Lewis, and D. W. R. Wallace (2006), MS Excel Program developed for CO_2 system calculations, *Rep. ORNL/CDIAC-105*, Carbon Dioxide Inf. Anal. Cent., Oak Ridge Natl. Lab., U.S. Dep. of Energy, Oak Ridge, Tenn.

Pierrot, D., C. Neill, K. Sullivan, R. Castle, R. Wanninkhof, H. Lüger, T. Johannessen, A. Olsen, R. A. Feeley, and C. E. Cosca (2009), Recommendations for autonomous underway pCO_2 measuring systems and data–reduction routines, *Deep Sea Res., Part II*, *56*, 512–522, doi: 10.1016/j.dsr2.2008.12.005.

Rösel, A., et al. (2016a), N-ICE2015 Snow Depth Data With Magna Probe, Norw. Polar Inst., Tromsø, Norway, doi:10.21334/npolar.2016.3d72756d.

Rösel, A., et al. (2016b), N-ICE2015 Total (Snow and Ice) Thickness Data From EM31, Norw. Polar Inst., Tromsø, Norway, doi:10.21334/npolar.2016.70352512.

Rysgaard, S., R. N. Glud, M. K. Sejr, J. Bendtsen, and P. B. Christensen (2007), Inorganic carbon transport during sea ice growth and decay: A carbon pump in polar seas, *J. Geophys. Res.*, *112*, C03016, doi:10.1029/2006JC003572.

Rysgaard, S., J. Bendtsen, L. T. Pedersen, H. Ramlöv, and R. N. Glud (2009), Increased CO_2 uptake due to sea ice growth and decay in Nordic Seas, *J. Geophys. Res.*, *114*, C09011, doi:10.1029/2008JC005088.

Rysgaard, S., J. Bendtsen, B. Delille, G. Dieckmann, R. N. Glud, H. Kennedy, J. Mortensen, S. Papadimitriou, D. N. Thomas, and J.-L. Tison (2011), Sea ice contribution to air-sea CO_2 exchange in the Arctic and Southern Oceans, *Tellus, Ser. B*, *63*, 823–830, doi:10.1111/j.1600-0889.2011.00571.x.

Rysgaard, S., R. N. Glud, K. Lennert, M. Cooper, N. Halden, R. J. G. Leakey, F. C. Hawthorne, and D. Barber (2012), Ikaite crystals in melting sea ice—Implications for pCO_2 and pH levels in Arctic surface waters, *Cryosphere*, *6*, 901–908, doi:10.5194/tc-6-901-2012.

Rysgaard, S., et al. (2013), Ikaite crystal distribution in winter sea ice and implications for CO_2 system dynamics, *Cryosphere*, *7*, 707–718, doi:10.5194/tc-7-707-2013.

Schuster, U., et al. (2013), An assessment of the Atlantic and Arctic sea–air CO_2 fluxes, 1990–2009, *Biogeosciences*, *10*, 607–627.

Serreze, M. C., and J. Stroeve (2015), Arctic sea ice trends, variability and implications for seasonal ice forecasting, *Philos. Trans. R. Soc. A*, *373*, 20140159, doi:10.1098/rsta.2014.0159.

Spreen, G., L. Kaleschke, and G. Heygster (2008), Sea ice remote sensing using AMSR-E 89-GHz channels, *J. Geophys. Res.*, *113*, C02S03, doi:10.1029/2005JC003384.

Takahashi, T., J. Olafsson, J. G. Goddard, D. W. Chipman, and S. C. Sutherland (1993), Seasonal variation of CO_2 and nutrients in the high latitude surface oceans: A comparative study, *Global Biogeochem. Cycles*, *7*, 843–878.

Takahashi, T., et al. (2009), Climatological mean and decadal change in surface ocean pCO_2, and net sea-air CO_2 flux over the global oceans, *Deep Sea Res., Part II*, *56*, 554–577.

Wanninkhof, R. (2014), Relationship between wind speed and gas exchange over the ocean revisited, *Limnol. Oceanogr. Methods*, *12*, 351–362, doi:10.4319/lom.2014.12.351.

Wanninkhof, R., and K. Thoning (1993), Measurement of fugacity of CO_2 in surface water using continuous and discrete sampling methods, *Mar. Chem.*, *44*, 189–204.

Wanninkhof, R. H. (1992), The relationship between wind speed and gas exchange over the ocean, *J. Geophys. Res.*, *97*, 7373–7382.

Weeks, W. F., and S. F. Ackley (1986), The growth, structure and properties of sea ice, in *The Geophysics of Sea Ice*, edited by N. Untersteiner, Plenum, New York.

Weiss, R. F. (1974), Carbon dioxide in water and seawater: The solubility of a non-ideal gas, *Mar. Chem.*, *2*, 203–205.

Weiss, R., and B. A. Price (1980), Nitrous oxide solubility in water and seawater, *Mar. Chem.*, *8*, 347–359.

Yager, P. L., D. W. R. Wallace, K. M. Johnson, W. O. Smith Jr., P. J. Minnett, and J. W. Deming (1995), The Northeast Water polynya as an atmospheric CO_2 sink: A seasonal rectification hypothesis, *J. Geophys. Res.*, *100*, 4389–4398.

Yasunaka, S., et al. (2016), Mapping of the air-sea CO_2 flux in the Arctic Ocean and adjacent seas: Basin-wide distribution and seasonal to interannual variability, *Polar Sci.*, *10*, 323–334.